Journal of
Materials Chemistry A

ROYAL SOCIETY
OF CHEMISTRY

PAPER

View Article Online
View Journal | View Issue

Check for updates

Cite this: *J. Mater. Chem. A*, 2026, **14**, 18742

Chemistry and electronic structure of AlInP (001) surfaces upon exposure to water and oxygen

M. A. Zare Pour, †[ab] I. A. Ruiz Alvarado, †[c] J. Diederich, †[def] M. N. Qaisrani, [g] S. Shekarabi, [a] J. Koch, [a] C. Höhn, [d] C. Dreßler, [gh] D. Friedrich, [d] W. Jaegermann, [i] R. van de Krol, [de] W. G. Schmidt, [c] A. Paszuk [b] and T. Hannappel *[ah]

Received 25th January 2026
Accepted 2nd April 2026

DOI: 10.1039/d6ta00726k

rsc.li/materials-a

For solar water splitting, semiconducting surfaces must be stable and able to efficiently transfer charge carriers across the semiconductor/aqueous electrolyte interface. Despite its ubiquitous use as the topmost layer in various record-breaking photoelectrochemical (PEC) devices, the initial interaction of the AlInP (001) with water remains unexplored. This study examines the interactions between atomically ordered AlInP (001) surfaces prepared with either phosphorus (P-rich) or indium (In-rich) terminations and reactive electrolyte species such as water and oxygen are examined. Using photoemission and reflection anisotropy spectroscopy combined with computational calculations, changes to surface states, chemistry, and near-surface band structure under representative adsorbate environments are investigated. Water dissociates on both terminations: on the P-rich surface, the Al and In sites are active, whereas on the In-rich surface, the In–In bonds dissociate promptly, increasing surface reactivity. Prolonged oxygen exposure causes surface reordering, resulting in a decrease in band bending from 1.00 to 0.85 eV on the P-rich and from 1.80 to 0.85 eV on the In-rich surface. Time-resolved two-photon photoemission measurements show that the near-surface band edges remain stable within 0.15 eV upon exposure to water and heat despite the work function increasing by 0.32 eV in UPS. Meanwhile, hydroxylation reduces surface dipoles. Initial O_2 exposure has little effect on the P-rich surface, but prolonged exposure leads to the dehydrogenatition of hydroxyls on the In-rich surface. DFT calculations indicate that the reactivity is dependent on reconstruction, showing that molecular water adsorption on the In-rich surface (−0.40 eV) is more favorable than on the P-rich AlInP (−0.23 eV). These findings provide a comprehensive understanding of AlInP (001) surfaces under conditions representative of PEC and other applications of III–V heterostructures.

1 Introduction

III–V compound semiconductors have been identified as promising materials for optoelectronic applications and are used extensively in devices such as light-emitting diodes, detectors, high-electron-mobility transistors, electro-optic modulators, photovoltaic, and photoelectrochemical (PEC) devices. These semiconductors play a key role in attaining record efficiencies in photovoltaic energy conversion; their tunability and good lattice matching make them particularly well-suited for multi-junction solar cells.[1–6] This is particularly relevant for ternary materials, such as III–P compounds, which exhibit high band gap tunability, facilitating efficient absorption over a wide spectral range of solar wavelengths and complementing their high electron mobilities. These properties make III–P materials exceptionally well-suited for their use in high-performance optoelectronic[7] and PEC solar-to-fuel conversion devices, achieving highest benchmarking efficiencies.[8–10]

---

[a] *Fundamentals of Energy Materials, Institute of Physics, Faculty of Mathematics and Natural Sciences, Technische Universität Ilmenau, 98693 Ilmenau, Germany. E-mail: thomas.hannappel@tu-ilmenau.de*
[b] *BMFTR Junior Research Group PARASOL, Institute of Physics, Faculty of Mathematics and Natural Sciences, Technische Universität Ilmenau, 98693 Ilmenau, Germany*
[c] *Theoretical Materials Physics, Department of Physics, Universität Paderborn, 33095 Paderborn, Germany*
[d] *Institute for Solar Fuels, Helmholtz-Zentrum Berlin für Materialien und Energie GmbH, 14109 Berlin, Germany*
[e] *Institute of Chemistry, Technische Universität Berlin, 10623 Berlin, Germany*
[f] *Frick Chemistry Laboratory, Princeton University, Princeton, NJ 08544, USA*
[g] *Theoretical Solid State Physics, Institute of Physics, Faculty of Mathematics and Natural Sciences, Technische Universität Ilmenau, 98693 Ilmenau, Germany*
[h] *Institute of Micro- und Nanotechnologies, Technische Universität Ilmenau, 98693 Ilmenau, Germany*
[i] *Surface Science Laboratory, Department of Materials- and Geosciences, Technische Universität Darmstadt, Darmstadt 64287, Germany*

† These authors contributed equally to this work.

The so-called window layer is a critical component in all state-of-the-art devices for solar energy conversion, as it selectively transports one type of charge carrier (here electrons) to the solid/liquid interface, while minimizing interfacial recombination.[11–13] This ensures efficient energy extraction through well-aligned heterointerfaces. This selective contact for charge carriers has been identified as a crucial factor in optimizing the efficiencies of III–V devices across various applications.[2,8,9,11–16] Aluminium indium phosphide (AlInP) has a tunable band gap (E_g) ranging from 1.35 eV to 2.45 eV, depending on its composition,[17–24] and it is used as a window layer in most high-efficiency III–V multi-junction devices. Since in PEC applications, AlInP is in contact with any applied catalysts, electrolytes and other structures, its stability and performance are important factors for further device improvements. The precise electronic structure at the interface – especially the alignment of conduction band (CB) and valence band (VB), and the density and distribution of defect states – governs charge carrier selectivity, interfacial recombination and, ultimately, device efficiency. However, the performance of such heterostructures can be severely limited by losses that originate at or near the surface, particularly when the AlInP window layer is only tens of nanometers thick and thus is dominated by surface and interface properties.

The interaction between AlInP surfaces and species such as water and oxygen is a largely unexplored area, especially with respect to surface oxide/hydroxide formation. This area is crucial because the AlInP window layer is the outermost layer in many III–V record devices, meaning that changes to its surface during operation are key for ensuring high device performance and stability. May *et al.*[8] reported a remarkable 14% unassisted solar-to-hydrogen (STH) efficiency using a functionalized AlInP surface in contact with an electrolyte within a III–V tandem structure. Many III–V materials are known to exhibit limited long-term stability in such reactive or corrosive environments, necessitating the use of protective layers to chemically passivate and secure them against corrosion and dissolution. A common protective layer is titanium dioxide (TiO_2), which is typically deposited *via* atomic layer deposition (ALD).[9] In the ALD process, reactive oxygen precursors such as water are commonly used, sometimes in conjunction with plasma excitation. This can result in the semiconductor's surface oxidising prior to the actual TiO_2 growth. The TiO_2/AlInP heterointerface constitutes a vital component of PEC devices, with examples achieving remarkable STH efficiencies close to 20%, approaching highest efficiencies that can be achieved.[9,25] Recently, Reith *et al.*[26] demonstrated the TiO_2/AlInP heterointerface engineering significantly enhances charge carrier extraction, the STH efficiency, and stability of the device. Formation of interfacial oxide species underneath grown TiO_2 layers can severely degrade device performance,[26] motivating investigation of the stability of AlInP window layers under initial interactions with water and oxygen.

The interaction of water and oxygen with III–P surfaces has been the focus of numerous computational and experimental studies, which have suggested specific reaction mechanisms and molecular dynamics on different surfaces.[27–33] Most investigations have primarily targeted binary III–V semiconductors, such as indium phosphide (InP) and gallium phosphide (GaP) surfaces, due to the longstanding challenge associated with preparing, characterizing, and simulating ternary compounds. Henrion *et al.*[34] demonstrated that at −173.15 °C (100 K), low coverages of H_2O on ultra-high vacuum (UHV)-cleaved InP (110) result in dissociative adsorption, forming In–OH and P–H bonds, which introduce midgap acceptor states that pin the Fermi level. As H_2O coverage increases, molecular water becomes the main adsorbed species, whilst maintaining the flat-band potential. During an annealing process, molecular water desorbs initially, followed by a phase reorganization towards non-stoichiometric indium oxide. These findings highlight transitions between adsorption regimes that influence the electronic properties of InP (110).[34] May *et al.*[35] demonstrated that indium-rich (In-rich) mixed-dimer InP (001) surfaces, when exposed to water, experience dissociative adsorption forming In–O–P bonds, as opposed to In–O–In. In contrast, H-terminated, phosphorous-rich (P-rich) surfaces are irreversibly etched by water. It was observed that O_2 attacks the In-rich surface more aggressively than H_2O, even disrupting its bulk optical transitions. The absence of detectable hydroxyl intermediates suggests that the dehydrogenation of adsorbed species occurs rapidly at ambient temperature. These findings on reconstruction-dependent reactivity have guided strategies for stabilizing InP-based photoelectrodes under aqueous environments.[35]

Wood *et al.*[27] conducted a density functional theory (DFT) analysis of complex oxygen- and hydroxyl-rich GaP/InP (001) surfaces, identifying four dominant local bonding motifs: M–O–M and M–O–P bridges on oxygenated surfaces, and M–[OH]–M bridges along with atop M–OH configurations on hydroxylated surfaces (M = Ga, In). Each topology yields a unique signature to the electronic density of states, thereby offering a clear structural framework for analyzing the spectroscopy of native oxide layers. Notably, the M–O–M bridge motif can generate localized hole-trap states when subjected to strain or chemical disturbances, providing an atomistic rationale for photocorrosion in III–V photoelectrodes.[27] Some of the present authors in ref. 31, utilizing DFT calculations, demonstrated that single H_2O molecules preferentially adsorb on three-fold coordinated In atoms on the In-rich InP (001) surface. Dissociative adsorption is found to be more favorable than molecular adsorption and upon dissociation, the hydroxyl group preferentially bonds to In–In dimers, while hydrogen adsorbs at the mixed-dimer P atom. Furthermore, the energy barrier for water dissociation progressively diminishes as coverage is increased. By increasing the water coverage, an attractive interaction between the water molecules determines the interface morphology. When the surface is rich in water (when thick water layers are formed), the reaction barrier for water dissociation reduces distinctly. The resulting interfacial dipole shifts the InP valence band maximum (VBM) toward more positive values with respect to the oxygen evolution potential, yielding overpotentials of ≈ 1.7–1.8 eV for oxygen evolution reaction and 0.2–0.3 eV for hydrogen evolution reaction. These findings underscore how water coverage and surface termination jointly tune the electrochemical behavior of III–V photoelectrodes.[31]

Only a few studies have explored the interaction between ternary III–P materials, such as AlInP and gallium indium phosphide (GaInP), with water and oxygen. Key studies conducted by some of the present authors in ref. 32 employed DFT to illustrate that on $Al_{0.5}In_{0.5}P$, Al–Al dimers within the second layer are preferred adsorption sites. These dimers create III–O bond states within the band gap, which can serve as surface-localized recombination centers. Calculations suggest that the early stages of oxygen adsorption do not result in the passivation of the III–V (001) surface states.[32] However, the AlInP surface reconstruction examined in the DFT study[32] differs from those prepared experimentally *via* metal–organic vapor phase epitaxy (MOVPE), which is a crucial point. Ostheimer *et al.*[36] investigated the interaction of GaInP (001) with water utilizing both experimental and *ab initio* molecular dynamics (AIMD) methods. They determined that water vapor interaction with GaInP (001) surfaces is markedly affected by surface reconstruction. Molecular adsorption is preferred on P-rich surfaces, while dissociative adsorption occurs on III-rich (4 × 2) terminations. Hajduk *et al.*[37] utilized soft X-ray photoemission spectroscopy (SXPS) to show that p-GaInP (001) with a native sub-monolayer oxide, when immersed in liquid water, forms Ga–OH, In–OH, and H–In–OH species. This transformation converts Ga oxides to hydroxides, occasionally leaving metallic Ga, and produces P–H bonds, elevating work function (Φ) by approximately 80 meV and altering the VB edge. The substitution of Al with Ga can lead to alterations in the surface's chemical properties, thereby influencing its reactivity, which emphasizes the necessity for a detailed examination of AlInP to allow for a more targeted design of this key III–V interface.

Understanding the surface reactivity as a function of AlInP surface reconstruction is crucial for preparing well-defined heterointerfaces and minimizing potential photovoltage losses. Therefore, it is essential to investigate how AlInP surfaces are modified upon exposure to water and oxidative environments. Such modifications can result in surface reconstructions, the quenching of defects, or the introduction of new recombination sites, potentially affecting the band gap surface states.[14] Hence, acquiring a comprehensive theoretical and experimental understanding of the electronic structure of AlInP surfaces and interfaces is crucial for further optimization III–V heterostructures, since both basic properties of clean and knowledge-based engineering of modified surfaces are vital for achieving maximal device efficiency.[38]

We employ a combination of experimental methods and DFT calculations to understand the modification of electronic structure and chemical composition of P- and In-rich AlInP surfaces upon oxidation. In particular, we explore how the early-stage interactions of the AlInP surface with H_2O and O_2 depend on surface reconstruction, which atomic motifs act as the initial reactive sites (P–P dimers *versus* subsurface Al/In sites *versus* In–In bonds), and how the resulting hydroxide/oxide species modify surface states and near-surface band energetics. Well defined surface reconstructions of AlInP prepared by MOVPE are examined before interacting with O containing species, as previously explored in detail by some of the present authors in ref. 16. Reflection anisotropy (RA) spectroscopy as a surface sensitive method is used to *in situ* monitor surface changes during initial stages of the interaction of water with the surfaces. We utilized photoemission spectroscopy (PES) to examine the alteration in chemical and electronic characteristics of AlInP surfaces upon exposure and oxidation utilizing its chemical and electronic information content. Additionally, time-resolved two-photon photoemission (tr-2PPE) measurements were employed to resolve near-surface electron dynamics. The adsorption of single water molecules, hydroxyls and O atoms on the P- and In-rich AlInP surfaces are investigated by DFT calculations. The calculations are compared to experimental measurements in order to understand the water interaction with the surface during initial exposure. The reconstruction-controlled "reactive-site" model developed here is expected to be broadly transferable to other III–V (001) surfaces. Here, surface reconstruction governs whether group-III back-bond sites, group-V dimers, or group-III–group-III motifs dominate the earliest hydroxylation/oxidation steps. In this sense, AlInP (001) is a model case that helps to connect previous observations on related III–P systems (*e.g.*, InP, GaP, or GaInP) that were dependent on surface reconstruction, including those by the present authors, to the resulting changes in surface state and band alignment that are relevant to PEC operation and ALD-based interface formation.

2 Results and discussion

2.1 Oxidation processes on P-rich AlInP (001) and their impact on near-surface electronic structure

The P-rich AlInP surface, prepared *via* MOVPE, has been thoroughly characterized previously as shown in ref. 16. AlInP with a P-rich termination features P–P dimers on the surface, with one P atom per dimer buckled by a hydrogen atom, resulting in a (2 × 2)-2D-2H surface reconstruction consisting of 2 dimers and 2 H atoms within each unit cell.[15,16,39] The modification of the P-rich AlInP surface is examined after different reactive stages: (i) the initial stages of interaction with water in vacuum, where the water dosage introduced to the surface is regulated by the partial pressure of water within the chamber at room temperature while monitoring surface changes *in situ*, followed by higher dosages of water, (ii) the surface is simultaneously exposed to heat (200 °C) and water to stimulate possible reactions similar to the ALD process. The following sections discuss the findings from these set of experiments. Additionally, analysis of the surface exposed to controlled amounts of O_2 in vacuum and finally, the surface in contact with liquid water and air can be found in the SI (Fig. S1–S3).

2.1.1 Water exposure of the P-rich AlInP surface. At first, we focus on the early stages of water-induced modifications of the P-rich AlInP surfaces. After MOVPE growth, the pristine sample is immediately transferred *via* a dedicated UHV shuttle to the UHV cluster with a base pressure on the order of 10^{-10} mbar, ensuring the sample remains free of C, O, and other contamination throughout the transfer process. Within the UHV cluster, the sample is introduced into a specially designed chamber for

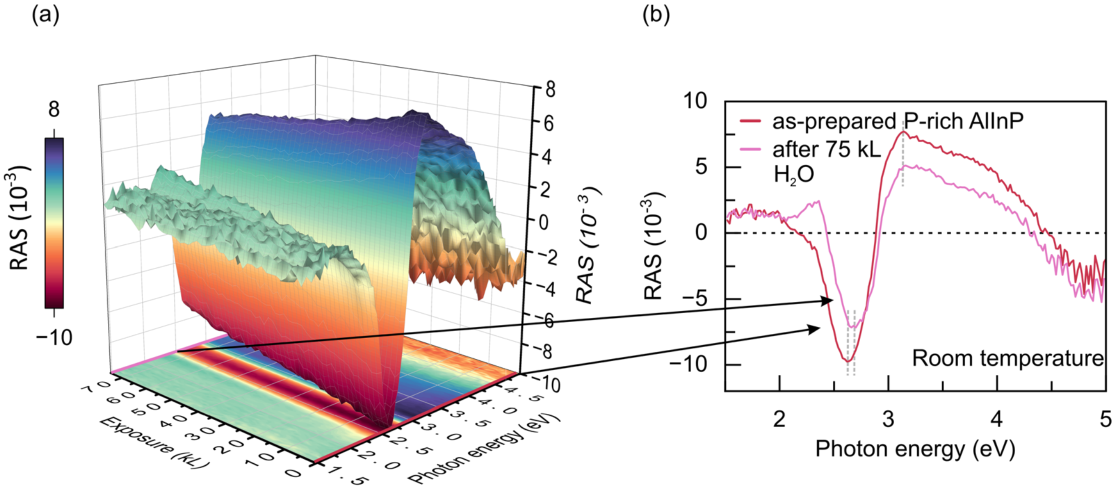

Fig. 1 (a) 3D color plot of *in situ* RAS measurement during exposure of 75 kL of water to P-rich AlInP (001) surface and (b) RA spectra measured at the beginning and end of the exposure. Red spectrum: as-prepared P-rich AlInP; pink spectrum: after 75 kL water exposure.

water exposure. This chamber is equipped with a water reservoir connected through a leak valve, which allows for the controlled delivery of water vapor dosage onto the surface by controlling the partial pressure and exposure time. Exposure is measured in Langmuir (L), with 1 L equal to 100 s at 1.3×10^{-8} mbar. RAS is employed as an *in situ* monitoring technique to capture early stage surface modifications and reaction processes. Before initiating water exposure, the RA spectra of transferred samples are measured to confirm P-rich, contamination-free surfaces and to serve as a reference for changes after water exposure. First, a total of 75 kL (47 min at 1×10^{-5} mbar + 11 min at 1×10^{-4} mbar) of water is exposed to the P-rich AlInP surface. Fig. 1 illustrates (a) a color plot of the RA spectra continuously recorded throughout the exposure process, providing a time-resolved view of spectral changes as the surface reacts with water molecules, and (b) representative RA spectra recorded at the beginning and the end of the exposure for direct comparison.

This 75 kL dose was chosen for saturation exposure at room-temperature in UHV. Water dosing continued until the *in situ* RA spectra stopped evolving, providing a reproducible endpoint for the "initial interaction" regime (*i.e.* early-stage hydroxylation/oxidation rather than deliberate growth of a thick oxide layer). The exposure experiment was ended by closing the leak valve, resulting in a rapid pressure drop from 10^{-4} mbar to low 10^{-8} mbar within a few seconds, effectively "freezing" the condition. Subsequently, the sample was promptly transferred to the PES chamber, where the pressure is maintained in the low 10^{-10} mbar range to facilitate a detailed post-exposure chemical and electronic analysis. To track chemical and electronic changes upon exposure, X-ray photoemission spectroscopy (XPS) measurements were performed on the samples before and after the exposure experiments.

Fig. 1 demonstrates that upon water exposure, only the peak around 2.60 eV in the RA spectrum shows a moderate reduction in intensity and undergoes a blue shift (shifting to higher photon energies), whereas the overall line shape of the RA spectrum remains unchanged. Previously, this feature at 2.60 eV was assigned to electronic transitions between electronic states localized at the partially hydrogen-terminated P dimers.[39] Reduced intensity of this feature suggests that the P–P dimers on the P-rich AlInP surface are only partially affected by water. In the scenario of complete surface dissociation, it is anticipated that the RA signal would reduce to zero.[35,40] Hence, the analysis of these spectra suggests that the surface structure remains largely unchanged under water exposure, though the intensity of spectral features decreases. Furthermore, the blue shift is particularly noticeable in the lower photon energy region of the spectrum. Modifications in the surface dipole may also contribute to this shift, as they can induce a linear electro-optic effect.[35,40,41]

Fig. 2 presents the XPS results acquired at an emission angle of 15°, enhancing surface sensitivity to effectively resolve low-concentration surface species. The initial characterization of the P-rich AlInP surfaces, represented by the red spectra, reveals a pristine surface free of C or O contamination, as confirmed by the survey spectra and the high-resolution (HR) scan of the O 1s core level in Fig. 2 (see Fig. S4(a) in the SI). The pink spectra correspond to the same surface after exposure to 75 kL of water.

To identify the nature of the oxygen species formed, the primary AlInP core levels – In $3d_{5/2}$, P 2p, and Al 2p – are further analyzed. Modification of the surfaces can results in changes of the energetic position of the Fermi level pinning and the band bending (BB), which induces shifts in core level energies. To sensitively resolve newly formed surface species, the spectral line shapes are compared before and after water exposure. To distinguish changes of chemical composition from core level shifts due to changes in the BB, all the XP spectra of In $3d_{5/2}$, P 2p, and Al 2p are normalized, with peak positions aligned to maximize spectral overlap, thereby presenting the *X*-axes in Fig. 2 as "relative binding energy." Furthermore, difference spectra *vs.* the as-prepared P-rich AlInP surfaces are plotted and scaled by a factor of two to emphasize the observed changes. Horizontal bars positioned above each spectrum illustrate the

(a) XP sepctra of core levels, excitation by mono. Al *Kα*, 15°

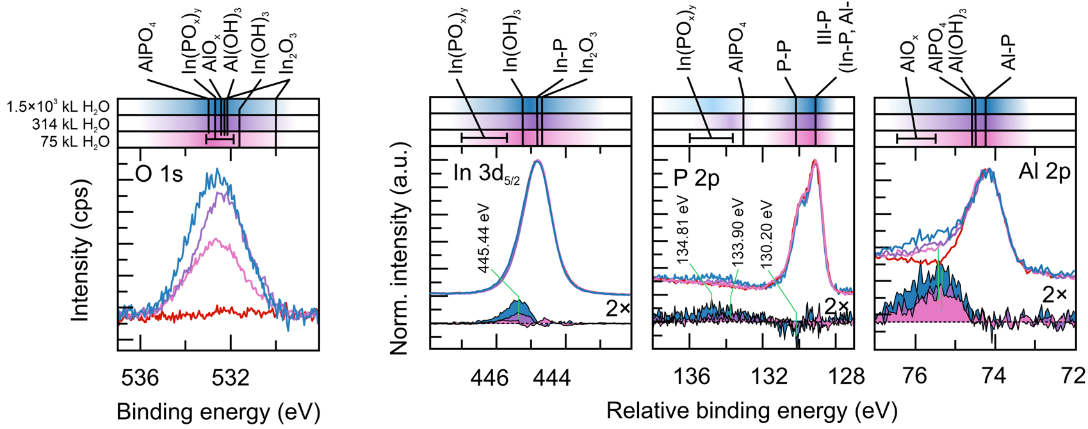

(b) UP spectra of VB, excitation by He II, *hν* = 40.81 eV

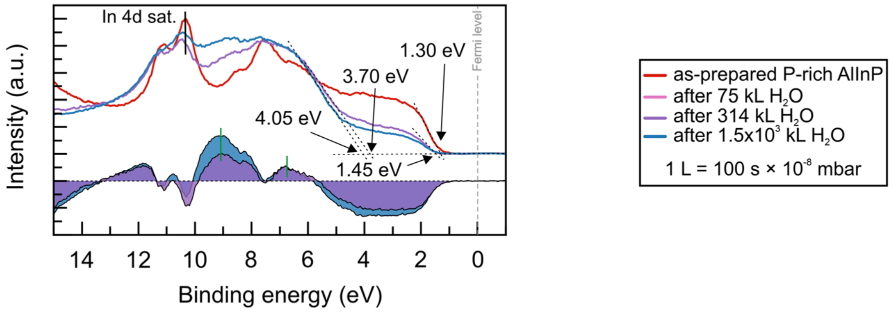

Fig. 2 (a) HR XP spectra of O 1s, In 3d$_{5/2}$, P 2p, and Al 2p core levels (left to right) for P-rich AlInP (001), recorded before (red) and after exposure to 75 kL (pink), 314 kL (purple), and after 1.5 × 10^3 kL (blue) of water. To demonstrate the spectral changes induced by exposure, In 3d$_{5/2}$, P 2p, and Al 2p core levels spectra are normalized to their respective maximum intensity, and the post-exposure spectra are shifted to maximize overlap with the as-prepared spectra. Accordingly, the *x*-axis is labeled as "Relative binding energy." Difference spectra *vs.* P-rich are multiplied to two and plotted. The horizontal bars positioned above each spectrum specify the BE ranges of various oxide species, serving as references to facilitate peak assignment. (b) The UP VB spectra with He II excitation of P-rich AlInP before and after exposure.

binding energy (BE) of various components, as reported in the literature.[42–58] A summary of these values is provided in the SI in Table S1. As depicted in the diagram, the contributions from various oxides and hydroxides are in very close proximity or overlap, making precise fitting both challenging and potentially unreliable. This challenge is enhanced by the low concentration of oxide species and the use of Al K*α* as an XPS source. Compared to synchrotron radiation with lower X-ray energy, Al K*α* has a lower surface sensitivity, which limits its ability to resolve low concentration oxides accurately while accounting for all possible contributions. It should also be noted that the complete formation of a stoichiometric oxide bulk phase with well-defined BE values may not occur in the experiments presented, as we attempt to simulate the early stages of water exposure, and do not optimize for oxide growth. This most likely results in BE values that are only qualitatively related to the respective bulk values due to the sub-monolayer or few-layer nature of created oxides. It is anticipated that increasing the dosage of water and subjecting the surface to more drastic oxidation will lead to the formation of lattices of different oxides and hydroxides, thereby bringing the BE of emission lines closer to literature values. In the following discussion, the likelihood of the presence of each component is assessed.

In Fig. 2(a), interestingly, the In 3d$_{5/2}$ and P 2p core levels do not exhibit significant changes of their line shapes after 75 kL water exposure (see the pink spectra). If P–P dimers were dissociated, a decrease in the signal at approximately 130.0 eV would be detected, along with a new components appearing between 133.9–136.0 eV in P 2p and 445.7–447.0 eV in In 3d$_{5/2}$.[45,58] However, such changes in the core levels are not observed, indicating that the surface has not undergone modifications leading to the formation of In(PO$_x$)$_y$ species with In–O–P bonds.[45,58] Similarly, the formation of In$_2$O$_3$ (In–O–In bonds) can be ruled out. Although the In–O–In emission line in In 3d$_{5/2}$ core level would appear at 444.7 eV, close to the In–P contribution, its presence would also result in O 1s signals at 530.0 eV and 532.7 eV (with full width at half maximum (FWHM) of 1.8 eV for each emission line),[35,45] which are not observed. A small quantity of In–OH cannot be entirely ruled out, since In(OH)$_3$ is known to appear at 445.2 eV in the In 3d$_{5/2}$ region and at 531.8 eV in the O 1s region,[45,58] overlapping with the In–P signal in the In 3d$_{5/2}$ core level and the identified peak in O 1s, respectively. However, if present, the concentration of In–OH is expected to be minimal. This is because a substantial concentration would result in an asymmetric profile of the In 3d$_{5/2}$ peak. This observation suggests that In–P sites in the first

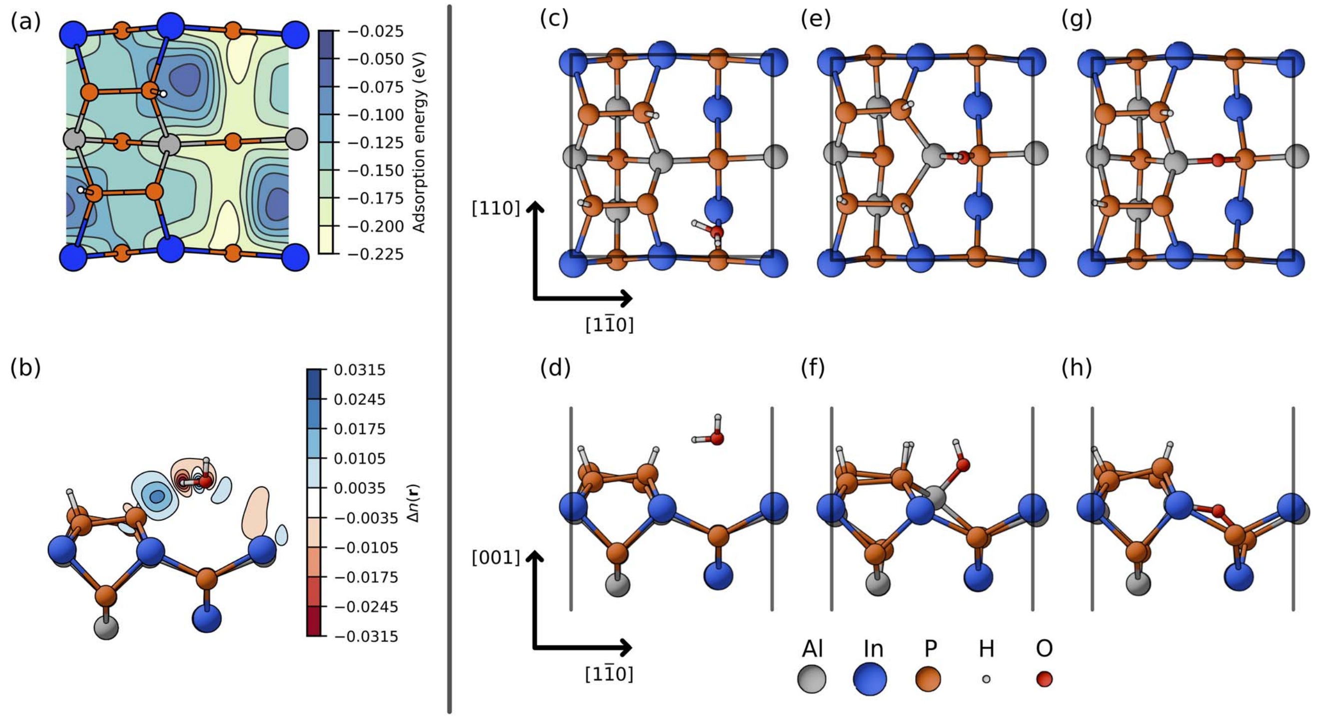

Fig. 3 Calculated potential energy surfaces for single water molecules on P-rich AlInP (001) (2 × 2)-2D-2H (a). A more negative adsorption energy indicates a more favorable adsorption site. Calculated water-induced charge redistribution for water adsorbed on (2 × 2)-2D-2H (b), blue and red isosurfaces signify areas of charge accumulation and depletion, respectively. Top (c) and side (d) view of the most energetically favorable structural configuration for a single adsorbed water molecule. Top (e) and side (f) view of the most energetically favorable structural configuration for an adsorbed OH group. Top (g) and side (h) view of the most energetically favorable structural configuration for an adsorbed O atom.

and the second monolayers do not serve as the most favorable site for the absorption of water molecules. Minor variations in In and P core levels remain within the noise level and do not conclusively indicate chemical changes by 75 kL water.

In contrast, a broadening at higher BEs in the Al 2p core level is observed, as evident in the difference spectrum, suggesting the formation of a new contribution upon water exposure. This contribution is only detectable at a 15° measurement and not at 90° (see Fig. S5 in the SI), appearing at roughly 75.3 eV as indicated by the green guideline in the difference spectrum. This BE correlates with values reported in the literature for non-stoichiometric AlO_x and Al–O–Al bonding configurations.[43,49] In the case of Al–O–Al formation due to water exposure, the presence of O-containing bonds requires detecting a correlated signal at 532.2 eV in the O 1s core level as well. The clear observation of a pronounced emission in this region after the exposure of 75 kL of water indisputably confirms that water molecules are dissociated and form Al–O–Al bonds. It should be emphasized that Al and In atoms located in the second and third monolayers from the surface are not entirely buried; rather, they remain exposed to the vacuum and are available for interaction with incoming species if such sites are reactive to the particular species (refer to Fig. 3(a) for a top view of the surface reconstruction; which will be discussed in the following).

The absence of a peak at 133.0 eV in the P 2p core level after only 75 kL water suggests that the formation of $AlPO_4$ (characterized by Al–O–P bonds)[42,47] can be excluded, though it is expected that some Al–OH bonds are formed on the surface.[48] The dissociation of water into OH^- and H^+, leading to the adsorption of OH^- on Al and In sites, and H on P sites (where P possesses dangling bonds on the P–P dimers at the surface), may constitute a viable mechanism for the formation of Al–OH and In–OH. The interaction between H and P does not lead to noticeable emission changes, because H has a minimal effect on P. Similar mechanisms are reported for interaction of water with other III–V surfaces.[35,59] Nonetheless, the inherent surface sensitivity and resolution limitations of XPS using a monochromatic Al Kα X-ray source must be considered, particularly when attempting to resolve low concentrations of P–O–Al and P–O–In bonds in the P 2p region. While considering hydroxylation, the potential formation of AlOOH and InOOH should also be taken into account. However, distinguishing these chemical states from other hydroxyl and oxides species remains challenging (check Table S1 to see their BEs in the SI).

To summarize, under the given water exposure conditions, these findings lead to several insights: (i) P–P dimers at the surface have not dissociated and do not serve as the primary active sites for water interaction in the first step; (ii) the initial interaction likely involves Al atoms located in the second or third atomic layers beneath the surface at the initial lower exposure; (iii) water molecules preferentially adsorb into surface valleys rather than undergoing direct chemical reactions at first monolayer sites; (iv) the surface experiences partial surface reordering; (v) hydroxylation occurs through the dissociation of water into OH^- and H^+, with OH^- adsorbing onto Al and In sites and H onto P; and (vi) the interaction between water and the surface is not in a steady state, additional exposure will further alter the surface chemistry. These observations are consistent with the prior work on the interaction of water with P-rich InP (001).[33] Both experimental results and DFT calculations indicated that on InP (2 × 2)-2D-2H and (2 × 2)-2D-1H surfaces, the most energetically favorable adsorption sites for water molecules are not the P–P dimers, but rather the valleys between them.[33] Furthermore, a previous work[32] has demonstrated that the oxidation of AlInP predominantly results in the formation of Al–O bonds rather than In–O bonds, aligning with the findings shown here for the initial low water exposure.

To investigate further surface modification through additional oxidation, a P-rich AlInP surface was exposed to 314 kL (purple, 68 min at 1×10^{-4} mbar) and 1.5×10^3 kL (blue, 129 min at 2×10^{-4} mbar after 314 kL) of water, see Fig. 2. However, the process was not monitored *in situ* by RAS. After 314 kL of exposure, spectral modifications are observed not only in the Al 2p but also in the P 2p and In $3d_{3/2}$ core levels. Analysis of the In $3d_{3/2}$ spectrum reveals an asymmetric feature at 445.4 eV, suggesting formation of $In(PO_x)_y$ components.[45,58] In the P 2p region, a decrease in intensity is noted at 130.2 eV, associated with contributions from P–P dimers, indicating partial dissociation of P–P dimers.[16,35] Additionally, an evolution of signal at 132.5–136.0 eV region, with a maximum at 133.9 eV is observed, which can be attributed to In–O–P ($In(PO_x)_y$)[45,58] and Al–O–P species.[42,47] Thus, these findings suggest the development of a mixture of both In–O–P and Al–O–P bonds. This interpretation is further supported by emissions detected in the O 1s region. The presence of In–O–In bonds, characteristic of In_2O_3, is generally unanticipated and will likely only occur at a very low concentrations, as evidenced by the lack of a 530.0 eV signal in the O 1s region.[35,45] The dominant Al-containing oxide species on the surface is Al–O–Al, as evidenced by the evolution of a signal around 75.50 eV in the Al 2p region and the peak with a maximum at 532.37 eV in the O 1s region.[43,49]

Increasing the water dosage to 1.5×10^3 kL leads to a higher concentration of oxide/hydroxide species on the surface. The peak intensity associated with oxide/hydroxide species in the O 1s spectrum not only rises but also exhibits an asymmetry change in addition to a chemical shift of peak maximum by 300 meV towards higher BEs, which aligns with the expected presence of In–O–P and Al–O–P.[45,58] Such a change in the asymmetry of the peak indicates changes in the ratio of different oxide/hydroxide types. The changes observed in In $3d_{5/2}$, P 2p, and Al 2p spectra are consistent with this observation. Notably, within the P 2p region, the peak maximum attributed to P-containing oxide species (highlighted in the difference spectrum) similarly shows an asymmetric change and shifts to 134.81 eV, indicating an increased In–O–P to Al–O–P ratio. This observation indicates a higher degree of oxidation of P atoms upon further exposure, potentially transitioning from P^{3+} to P^{5+}.[60–64] The formation of P–OH on the surface might be considered; however, as these species are anticipated to emerge at approximately 132.30 eV, where no emissions are detected, their presence is unlikely or minimal.[65] The increase in emission at 75.50 eV within the Al 2p spectrum, particularly linked to the Al–O–Al bonds, indicates a heightened concentration due to prolonged exposure. The results shown here seem to support the formation of a mixture of non-stoichiometric In–O and Al–O species.

Fig. 2(b) illustrates the VB cutoff of the UP spectra for P-rich AlInP, depicted both before (red) and after exposure to 314 kL (purple) and to 1.5×10^3 kL (blue) of water using He II light. Exposure to 314 kL of water results in a notable decrease in emission below 5 eV as indicated in the difference spectrum, associated with the surface states of P-rich AlInP surface, as well as P dangling bonds. Although emission in this region is decreased, it is not entirely eliminated, indicating that surface states are only partially removed. This observation aligns with the XPS analysis, which shows a decreased emission line at 130.20 eV in the P 2p core level, indicating the partial dissociation of P–P dimers and consequently a reduction in the density of surface states linked to these dimers. In ref. 16, the analogies between P-rich InP and AlInP surface VB is discussed. Moreover, the observed decrease in surface states for P-rich AlInP upon exposure parallels the findings following the initial water pulse in the ALD process on P-rich InP, as detailed in ref. 66. As a result, the VBM of AlInP shifts from 1.30 eV to 1.45 eV below the Fermi level. It indicates that the BB in AlInP decreases from 1.00 eV on the P-rich surface to 0.85 eV after water exposure. The fact that P–P dimer contributions remain visible in the P 2p region, together with the VBM of AlInP located just 1.45 eV below the Fermi level which implies an upward BB towards the surface, support the conclusion that some defect surface states remain preserved, pinning the Fermi level.[16]

Upon examining the difference spectra in Fig. 2(b), two emission lines located at approximately 7 eV and 9 eV (highlighted by green lines) are observed as the sample is subjected to water exposure. It is known that OH^- species exhibit emission lines in this region[34,67,68] where the 1π and 3σ orbitals of adsorbed OH^- contribute to emissions near 8 and 10 eV. Larsson *et al.*[68] proposed that these emissions correspond to OH^- species at bridge sites between the first and second monolayers of the surface. Hydroxylation of the III–V surface when exposed to water has been previously reported, demonstrating that hydroxyl groups remain stable up to 400 °C.[59] While considering hydroxylation, the potential formation of AlOOH and InOOH should also be taken into account. However, distinguishing these chemical states from other hydroxyl species and oxides remains challenging.

Although certain VB features are identified and correlated with the formation of OH^- species, which are well-documented, the identification of different species based on the ultraviolet photoemission spectroscopy (UPS) necessitates an emphasis on two parameters that influence the VB features and the overall UP spectra: (i) the reduction of emission from the AlInP surface and (ii) the evolution of emission from newly formed oxide and hydroxide species. In some BEs, these two parameters can intersect and potentially counteract each other's effects, thereby complicating the evaluation of VB modifications and introducing a level of uncertainty. For instance, the emission from the VB of various oxide species identified by XPS (*e.g.*, In–O, Al–O, In–O–P, *etc.*) is expected to emerge within this BE region, resulting in overlapping emissions that complicate precise evaluation.

The emission occurring in the 10–12 eV range, which is attributed to the In 4d satellite, decreases slightly after 314 kL exposure; however, it increases again with 1.5×10^3 kL water exposure. This suggests that the emission of the In 4d satellite overlaps with the emissions from oxide species that become more prevalent with prolonged exposure. The VBM of the oxide becomes more pronounced after 1.5×10^3 kL exposure. By extrapolation, the VBM is determined to be 4.05 eV below the Fermi level. The Φ of the sample, based on the secondary electron cut-off measured with UPS, changes from 4.30 to 4.10 eV. Typically, an increase in Φ upon oxidation is anticipated,[69] but this is not observed here. On the surface of the clean P-rich AlInP, a net dipole forms due to surface P–P dimer layer for this surface reconstruction. Upon water exposure, these dipoles are altered and new dipoles form as various oxide and hydroxide species form. An exact prediction is challenging due to the complexity introduced by the modification of the surface through oxidation and hydroxylation.

To corroborate the experimental observations, DFT calculations were employed to determine the water adsorption configuration on the P-rich surface, denoted here as the (2×2)-2D-2H reconstruction. The potential energy surface characterizing single water molecule adsorption on the AlInP (001) (2×2)-2D-2H surface is depicted in Fig. 3(a). A more negative value of the adsorption energy implies more favorable adsorption conditions; thus, the most favorable adsorption sites can be identified as the brighter spots in the diagram. The differences in adsorption sites and energies are minimal when compared to InP P-rich surfaces, which aligns with established expectations.[33] Overall, intact water molecules adsorb favorably everywhere on the AlInP 2D-2H surface, with the most favorable sites having an energy of −0.23 eV. Notably, the P–P dimer is less favorable than other sites for water bonding. These observations are consistent with prior research on In-rich InP surfaces,[29,32] which demonstrated that water molecules preferentially adsorb at In sites rather than P sites. Similarly, on the AlInP (2×2)-2D-2H surface, the water molecule exhibits a preference for adsorption on top of the trench near Al and In atoms, with negligible energy differences observed between adsorption at Al and In sites, slightly favoring sites near In by 0.02 eV. The most favorable adsorption configuration is shown in Fig. 3(c) and (d). The water O atom faces the exposed surface In atom, while one of the water *H* points towards the undercoordinated P atom of the P–P dimer and the remaining H upwards normal to the surface. The surface geometry remains mostly intact, with molecular water adsorption only slightly disturbing the atoms from their ground state positions. It is worth mentioning that only one possible (2×2)-2D-2H surface is considered here for DFT calculation. As shown in ref. 39, a different subsurface ordering could be present which would result in Al always interacting with water like CuPt–B ordering (it refers to a cation ordering along the ⟨111⟩ direction in III–Vs' lattice) or the D4-C (please see ref. 39 for more details about these surface structures).

Fig. 3(b) depicts the minimum-energy geometry of a water molecule adsorbed on the surface, combined by the calculated charge redistribution caused by this adsorption. There is a modest charge accumulation between the water's H and the P atom in the P–P dimer, alongside a relatively weaker charge accumulation between the water's O atom and the second-layer In atom, resulting in weak physisorption. Calculated electronic structures indicate that water adsorption does not introduce additional states within the band gap, and that the states near the band gap are unchanged from the clean surface (*cf.* Fig. S7(a) and (b) in the SI). Indications of water dissociation on AlInP suggest that the presence of Al—particularly Al–P bonds – may facilitate dissociative adsorption, possibly by stabilizing intermediate hydroxyl species or lowering the activation barrier for O–H bond cleavage. Indeed, DFT calculations reveal that Al plays an important role for the dissociation process together with P–P dimers. This is consistent with previous theoretical study where Al atoms where found to oxidize faster than In.[32]

To gain further insight into interfacial water behavior under realistic conditions, we performed AIMD simulations of the solvated (2×2)-2D-2H P-rich AlInP (001) surface at 76.85 °C (350 K) (see Note S1 in the SI). The trajectory was analyzed to characterize the structural organization and dipole orientation of interfacial water layers. The density profile (Fig. S8(b) in the SI) confirms that water adsorption is localized above the dimer trenches, with the first hydration layer forming in the trench in between the P–P dimers. This layer remains molecular and non-dissociative throughout the 20 ps trajectory. Moreover, on average, water molecules dipoles are aligned with their oxygen atoms directed toward the surface. This behavior aligns well with the single-molecule $T = -273.15$ °C (0 K) adsorption geometry. The structural stability and orientational ordering suggest that the surface is chemically passive under these conditions.

Dissociative water adsorption was considered for an OH and H at the surface simultaneously, therefore the adsorption energy was calculated with eqn (2) (see Section 4.2) and $E_A = E_{H_2O}$. Fig. 3(e) and (f) show the most stable configuration for an OH adsorbed at the AlInP (2×2)-2D-2H and a H at one of the P–P dimers. This configuration presents an adsorption energy of −0.26 eV, slightly more favorable than the adsorption of the intact water molecule. Consequently, the proposed scheme during the first stages of water dissociation is for one of the H atoms to dissociate from the H_2O molecule and adsorb at the P-dangling bond and the OH^- at the exposed second-layer Al atom. Unlike molecular adsorption, the hydroxide modifies the surface geometry by pulling the Al upwards. Similarly, the extra H, pushes the P downwards to the same height of its counterpart on the P–P dimer. Furthermore, the electronic structure is modified as the highest occupied states is pushed down in energy. More notably the VBM originally found between Γ–J, is now located below the bulk VBM (see Fig. S7(c)). This surface orbital is related to the σ – like bonds between second row Al/In and the top P atoms (Fig. S7(e)). The shift in energy is a direct result of the OH bonding at Al atoms. Furthermore, the shift at point *K* is due to H passivating one the P dangling bonds (Fig. S7(f)) that are related to this state.[15,39] This could help to explain the decrease in the negative peak observed located at 2.6 eV in the RA spectra after water exposure in Fig. 1, as it is directly related to the P dangling bond.[16,39] Overall the E_g increases by ~0.2 eV. Interestingly, the lowest unoccupied states remain largely intact throughout the reciprocal space. It is important to mention that OH adsorption was only found to be energetically favorable when an H atom also adsorbs at the surface.

Oxidation from water exposure was also modeled by calculating a single O atom adsorbed at the surface and assuming the desorption of both H atoms. Here, the adsorbate energy in eqn (2) (see Section 4.2) is defined as the energy difference between water and hydrogen molecules, *i.e.*, $E_A = E_{H_2O} - E_{H_2}$, where the later term is the total energy of a free H_2 molecule. The most favorable O adsorption geometry is shown in Fig. 3(g) and (h). This configuration presents an adsorption energy of −0.37 eV, about 0.1 eV larger than the adsorption of an intact water molecule. The O bonds between the second and third layers of the 2D-2H surface forming an Al–O–P bond. Interestingly, the AlInP surface remains largely intact, only perturbing the atoms involved in the Al–O–P bond. The band gap is virtually the same only decreasing by 0.01 eV compared to the clean surface. However, the band structure is modified by lowering the dispersion of the P dangling state[15,39] between *k*-points *Γ* and *J*, see Fig. S7(d). Nevertheless, there are no additional states introduced in the band gap that otherwise might affect the BB.

These observations align well with the experimental data. While Al atoms predominantly interact with water, a slight increase in water dosage also leads to the involvement of In atoms in the interaction with water. A possible water dissociation reaction would be for OH^- to adsorb at the second layer Al atoms and the H on the dangling bond of P–P dimers. Afterwards, the two hydrogen may desorb from the surface and consequently form an H_2 molecule leaving behind an O which forms an Al–O–P bond at the surface. Experimentally Al–O–P bonds were only observed after increased exposure to water, thus the oxidation of the Al–P bonds could be associated with large energy barriers that hinder the reaction. Additionally, dissociation of water and adsorption of OH^- on the surface can impact the situation by changing the adsorption landscape as the surface exposure to water is increased, as demonstrated for InP.[33] Furthermore, hydrogen-related defects could play a similar role in the dissociation of water as those observed on the InP surface. In this scenario, H atoms are likely to adsorb onto the phosphorus dangling bonds of the (2 × 2)-2D-1H P–P dimers. This adsorption would potentially result in partial passivation of the associated surface states, thereby contributing to a decrease in the BB.

To assess the impact of water-induced surface modifications on the electronic structure, the surface energy band diagrams of the P-rich AlInP before and after exposure to 314 kL and 1.5 × 10^3 kL of water, based on the experimental data, are illustrated in Fig. 4(a–c), respectively. In Fig. 2, the VBM of AlInP is observed to rise from 1.30 eV on the pristine surface (a) to 1.45 eV following exposure to 314 kL water (b) and remain stable at higher dosages of water (c). To determine whether this initial alteration can be attributed to modifications in the BB, the peak maximum positions of core levels are monitored both before and after a 1.5 × 10^3 kL H_2O exposure at emission angles of 90° and 15°, as detailed in Table S2 in the SI. Evidently, all core levels, along with the VBM, are shifted by approximately 200 meV towards higher BEs after exposure. Given the uniform

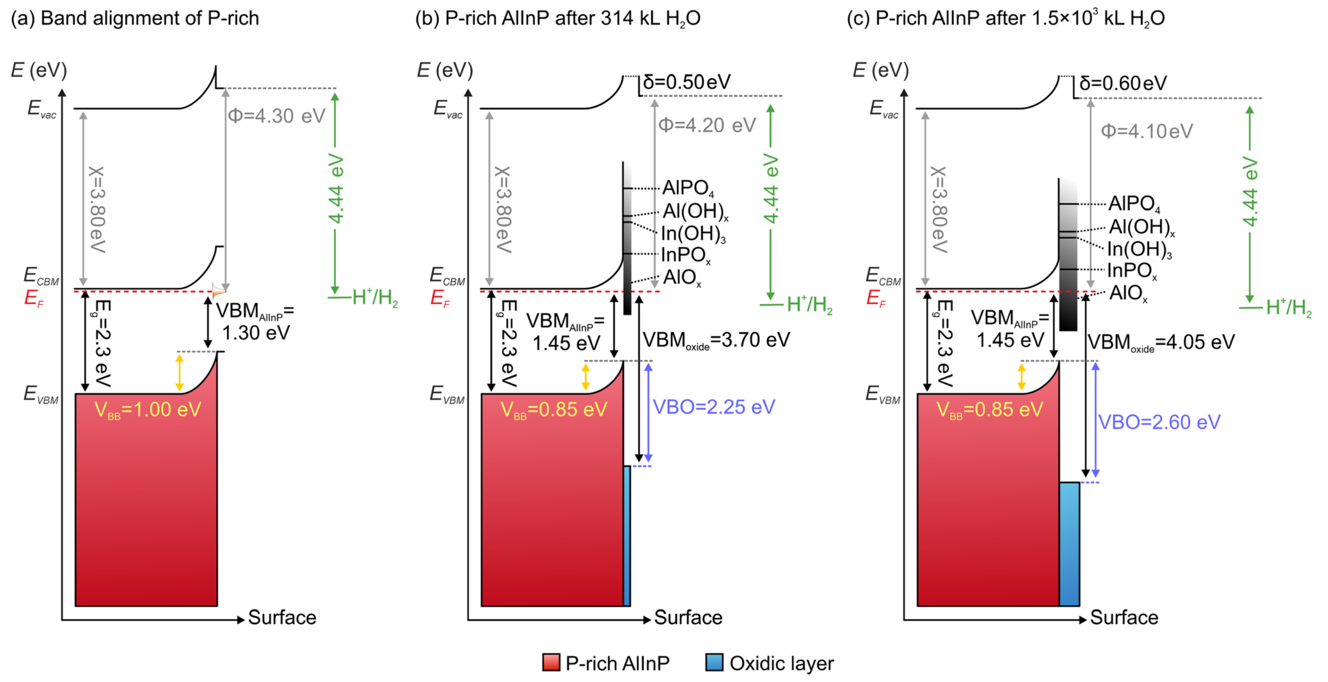

Fig. 4 The band alignment of P-rich AlInP before (a) and after 314 kL (b) and 1.5 × 10^3 kL (c) water exposure.

shifts observed in core levels as well as the VBM, it can be concluded that the magnitude of upward BB towards the surface is reduced to 0.85 eV. Nevertheless, the presence of upward BB is still detectable by comparing the XPS post-exposure results at angles of 90° and 15°, where a decrease in emission angle displays a shift of core levels towards lower BEs. For further details on the determination of band alignments, please refer to Note S2 in the SI.

The VBM of the oxide/hydroxide covered surfaces reaches 3.70 eV after 314 kL exposure (see Fig. 2(b), purple spectrum). After exposure to 1.5×10^3 kL, the VBM of oxides/hydroxides increases to 4.05 eV (see Fig. 2(b), blue spectrum). Considering the band gaps of various oxide species, the positions of their conduction band maximum (CBM) are determined and depicted in Fig. 4(b) and (c). As the water dosage is increased, the VBM of the oxides/hydroxides undergoes a shift, which simultaneously influences the position of the CBM. The band gaps of oxides/hydroxides can be significantly affected by their phase and stoichiometry, leading to uncertainty in accurately determining the exact location of the CBM of oxides/hydroxides. Owing to the presence of a thin oxide/hydroxide containing surface layer, achieving precise determination of these parameters is challenging. Consequently, Fig. 4 provides only a schematic representation of the band diagram.

The variation in the VBM of the oxides measured at 3.70 eV after 314 kL and 4.05 eV following 1.5×10^3 kL, compared to AlInP's VBM of 1.45 eV, establishes the valence band offset (VBO) at the AlInP/oxide interface. This VBO is determined to be 2.25 eV after 314 kL and rises to 2.60 eV after 1.5×10^3 kL. This may suggest the formation of additional donor states within the oxide layers, resulting in a more n-type characteristic as oxide formation progresses further. Given that the layer may interface with an electrolyte in water-splitting applications, the relative position of the H^+/H_2 potential is shown in green in Fig. 4.[70] However, this alignment requires careful consideration because even a small presence of adsorbates from the electrolyte can significantly alter the ionization potential. This shift may affect the precise placement of the electrode's electronic states relative to the electrolyte's redox potentials. Reference values, determined without contact formation, could be displaced owing to additional electrochemical dipolar potential drops. In the present band alignment, because the CBM of AlInP and the Fermi level are positioned just above the H^+/H_2 potential, this configuration suggests a favorable band alignment for hydrogen evolution reactions. However, the impact of oxide species on charge separation strongly depends on their chemical nature and the thickness of the oxidic layer. If the oxidic layer remains thin, and below the critical tunneling thickness, its presence may have a limited effect on charge carrier transfer. In contrast, a thicker oxidic layer, particularly in combination with a large conduction band offset (CBO), can act as a barrier to charge transport and contribute to photovoltage losses. The function of n^+-AlInP as an electron-selective contact further enhances the separation of charge carriers and promotes the transport of photo-generated electrons towards the surface, where the electrochemical reduction of H^+ to H_2 takes place.

The band diagram conveys essential information regarding the electronic structure of the material. It illustrates the relationship between the energies of electrons and the allowed electronic states within the material. The positions of the CB and VB, along with the band gap, reveal critical insights into charge carrier behavior, conductivity properties, and potential applications of the material in electronic devices. Additionally, the diagram may indicate the influence of doping, defects, or external factors on the energy levels, thereby aiding in the understanding and optimization of the material's performance in various technological contexts. The measured data might indicate the presence of an energy barrier for electron transport across the n-AlInP/oxide (or hydroxide) interface layer, attributed to the remaining depletion layer in the AlInP. Table S3 in the SI summarizes the elemental atomic concentration (%) before and after subjecting P-rich AlInP to varying doses of water, based on XPS measurements at 90° emission angle. The O atomic concentration is observed to rise from 3.9% after 75 kL of water exposure to 6.4% after 314 kL, eventually reaching 7.4% following the dose of 1.5×10^3 kL. Assuming the formation of a uniform layer, the oxide/hydroxide thickness after 1.5×10^3 kL water exposure is estimated to be below 3 Å, which is less than a full monolayer.

To summarize, RAS analysis during the initial water exposure to 75 kL showed minor spectral alterations, implying limited surface modification and preservation of P–P dimers. XPS data support this observation, indicating minimal shifts in the In and P core levels but identifying Al–O–Al bonds formation, as indicated by the appearance of new features in the Al 2p and O 1s regions. With higher water exposures (314 kL and 1.5×10^3 kL), more pronounced chemical changes occurred, including partial dissociation of P–P dimers and the formation of In–O–P and Al–O–P bonds. Overall, the study reveals that water initially interacts with subsurface Al sites rather than P dimers, and that oxidation progresses gradually proceed with increasing water exposure, resulting in the formation of ultrathin oxidic layers. UPS measurements indicated partial reduction of surface states and shifts in the VBM and Φ, reflecting a reduction in BB and changes of the electronic structure. Despite the reduced BB, its presence indicates only a partial elimination of AlInP surface states. This implies that depending on the application, distinct strategies should be considered for the electronic passivation of the AlInP surface. Moreover, the band diagram post-exposure is illustrated, revealing a CBO reaching up to 2.60 eV. If the oxidic layer exceeds the critical thickness for tunneling, this offset may influence charge separation mechanisms, potentially hindering electron transport across the interface. It should be mentioned at this stage that the investigation of changes induced by water exposure just presents the initial modification of the surface. Exposure to electrolyte may further modify the surface conditions.

2.1.2 Combined water and heat exposure.

To correlate exposure experiments with the ALD process, an as-prepared P-rich AlInP surface (without any prior water exposure) was subjected to water pulses while the substrate was heated to 200 °C. The duration of each pulse was set to match the time used in TiO_2 deposition. This condition is referred to as "water and heat

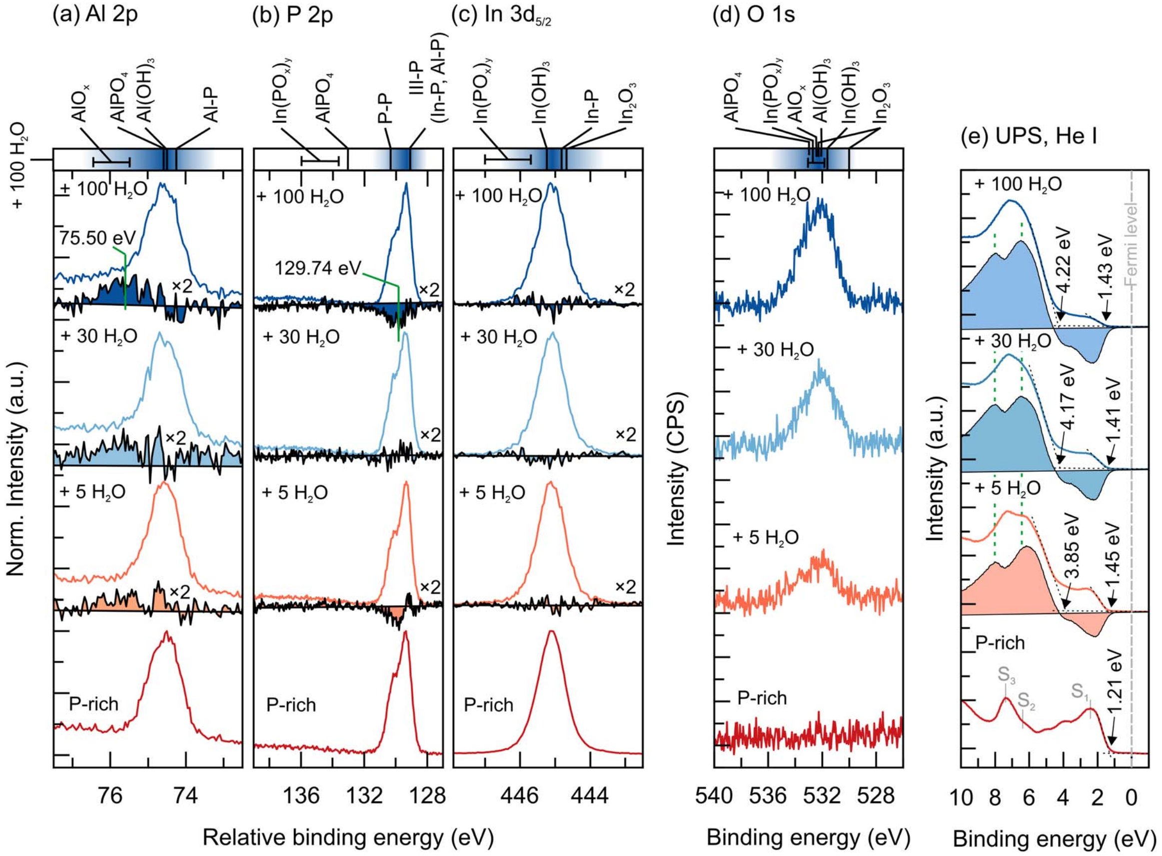

Fig. 5 XPS and UPS measurements upon water and heat (200 °C) exposure. XPS measurements are done at 90°. As-prepared P-rich AlInP, after 5, 30, and 100 water pulses spectra are shown in red, orange, light blue, and dark blue, respectively. (a–c) Are Al 2p, P 2p, and In $3d_{5/2}$ core levels where different spectra *vs.* P-rich are plotted and to investigate changes in spectral line shape, the spectra are normalized to 1 and shifted to maximize the overlap and therefore *X*-axis are "relative binding energy." (d) is O 1s core level and not normalized to show the evolution of O on the surface. The horizontal bars positioned above each spectrum specify the BE ranges of various oxide species, serving as references to facilitate peak assignment. (e) UP spectra with He I excitation. For comparison, the difference spectra *vs.* as prepared surface (P-rich) is plotted.

exposure." Fig. 5 presents the XPS and UPS results of this experiment, where 5 (orange), 30 (bright blue), and 100 (dark blue) pulses of water – a cumulative total of 135 pulses – were applied to the P-rich surface (red). Here, 5, 30, and 100 pulses (in total 135 pulses) are equivalent to water dosages of 5.5×10^6 L, 3.8×10^7 L, and 1.5×10^8 L, respectively. After each stage, the sample was transferred to the analysis chamber for PES and tr-2PPE measurements. The Al 2p, P 2p, and In $3d_{5/2}$ core levels are depicted in (a–c), with difference spectra plotted *vs.* the as prepared surface (P-rich).

Similar to the observation in the previous section, evolution of a new emission at 75.50 eV in the Al 2p line (indicated by the green guideline) becomes evident following 30 and 100 pulses which is correlated to the formation of Al–O–Al. The peak maxima of O 1s at *ca.* 532.10 eV support the formation of these bonds. Furthermore, examining the alterations in the P 2p spectra, an asymmetric decrease around 129.74 eV is noted, indicating the partial dissociation of P–P dimers. This asymmetry arises from the overlap of the $2p_{3/2}$ and $2p_{1/2}$ states. However, despite this observed decrease in the P 2p spectra, no noticeable increase in P 2p at a BE of 132–136 eV was detected, where one might expect the presence of P–O or Al–O–P. The induced asymmetry observed at higher BEs of the Al 2p line in addition to the BE range of O 1s emission line suggests the formation of Al–OH as a result of water and heat exposure.[48] This hypothesis is supported with UP spectra obtained post-exposure, where the appearance of emission lines at 6.50 and 8.20 eV are commonly linked to OH^- groups[34,37,67,68] (the emission lines are more clearly visible in the difference spectra in Fig. 5(e), where they are highlighted by green dashed lines). Hydroxylation of In may also occur as these VB features can similarly relate to In–OH. Given the absence of significant spectral changes in the In $3d_{5/2}$ core level, it becomes evident that Al undergoes hydroxylation more extensively than In. This inference is supported by Al's greater affinity for O. Apart from In–OH, no other In-containing oxide compound was detected by PES, or their presence lies below the detection limit. This implies that a fully oxidized layer is not formed.

Inspecting the UP spectra in Fig. 5(e), it is evident that the surface undergoes modification after 5 pulses. To facilitate comparison, the difference spectra *vs.* the P-rich surface are depicted, parallel to the UP spectra following exposure. In line with observation in the previous section, water rapidly modifies the P-rich surface, as indicated by partial elimination of surface states. Additionally, there is an emerging emission above 4 eV, where P-rich characteristic features either disappear or overlap with the rising VB features of oxides/hydroxides. As the number of water pulses increases, the emission above 4 eV becomes more pronounced, which is associated with the formation of oxide/hydroxide species on the surface. Considering the inelastic mean free path (IMFP) of UPS with He I excitation (0.5–1 nm), the VBM of the AlInP surface under the oxide/hydroxide species/layer remains observable, suggesting that the formed oxidic layer is still relatively thin, and the VBM of AlInP (underneath the oxidic layer) can still be measured. The AlInP VBM shifts from 1.21 eV to 1.45 eV after 5 pulses and remains there even with more water pulses. This shift is attributed to a decrease in the density of surface states, resulting in a reduction of upward BB magnitude. With further water exposure, the UP spectra transforms towards the VB characteristic of oxide species, with the VBM of oxides/hydroxide determined to be at 4.22 eV.

Beyond static band alignments, ultrafast carrier dynamics near the band gap and changes in the photoemission threshold provide deeper insight into how water exposure modifies the near-surface electrostatic environment and electronic states relevant to surface reactions. We performed tr-2PPE measurements (Fig. S16) on the P-rich AlInP (001) surface after each level of H_2O exposure at 200 °C. The resulting spectra and ultrafast dynamics (Fig. 6 and 7, as well as Fig. S10–S13 in the SI) reveal distinct changes in near-threshold photoemission and carrier relaxation that correlate with the PES observations of surface composition and electronic structure. Data is given up to 3.5 ps to show the relevant time-dependent features; the set-up is limited to 50 ps, so slower relaxation processes may not be captured. These measurements allow us to track how surface dipoles evolve under water/heat treatment and how the near-surface CBM states respond. tr-2PPE spectra are plotted against the Fermi level (from UPS Φ data, Table S4) to allow for the energies of initial states to be more directly apparent.

On the bare P-rich AlInP surface before water exposure, two primary photoemission features are observed, as reported in ref. 16: a CBM-related peak at an emission energy of 0.74 eV *vs.* E_F, and a broader mid-gap emission near the Fermi level, arising from surface/interface states that pin E_F. These mid-gap states are already occupied (due to Fermi-level pinning) and can be emitted by the probe photon alone, thus producing a strong one-photon photoemission signal. Accompanying these features is a well-defined low-energy cut-off in the photoelectron spectrum, corresponding to about 0.56 eV below the nominal vacuum level (all emission energies are reported with a +1.0 V sample bias correction to enable detection of electrons with low kinetic energies). Varying the detection bias confirms that this cut-off is an intrinsic surface property, *i.e.*, a real vacuum-level shift rather than an instrumental artifact. At a reduced bias of +0.2 V (Fig. S10(a) in the SI), the cut-off vanishes, yet it reappears at the same energy (relative to vacuum) when the bias is increased to +3.0 V (Fig. S10(b)). Thus, the ~0.56 eV cut-off reflects a modest surface barrier present on the clean P-rich surface, not a detector threshold. We attribute this initial

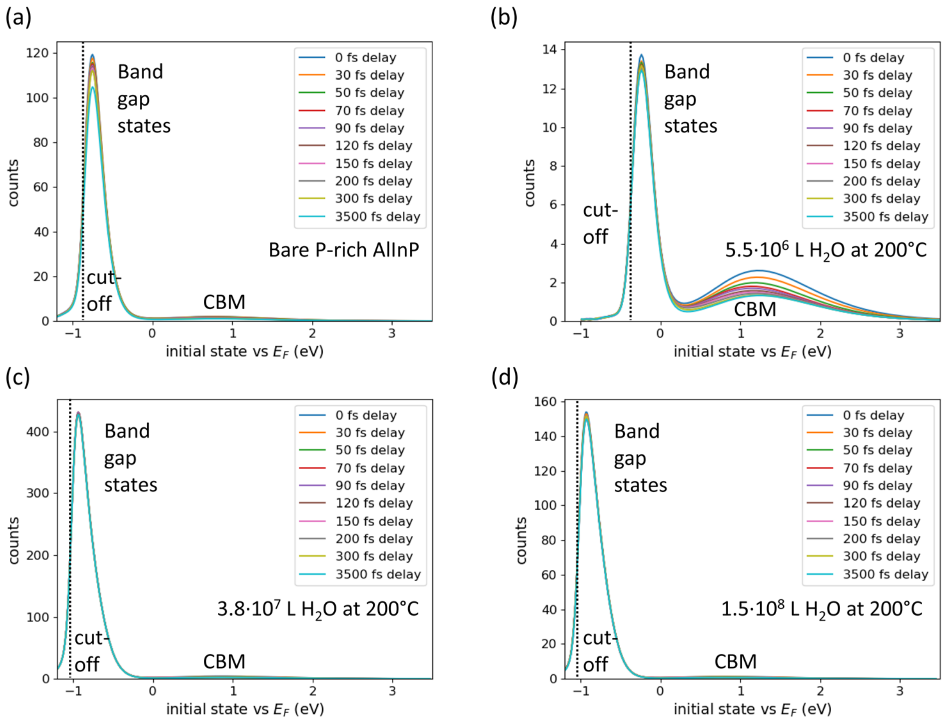

Fig. 6 Tr-2PPE spectra of the bare P-rich AlInP surface (a) and after 5 (b), 30 (c), and 100 pulses (d) of water exposure at 200 °C. Emission from the CBM is significantly lower than that from mid-gap states. The CBM emission intensity remains within a factor of ~2, whereas emission from mid-gap states varies more strongly due to the evolving low-energy cut-off. The initial energy of states that are then photoexcited is given *vs.* the Fermi level in the x-scale on each image.

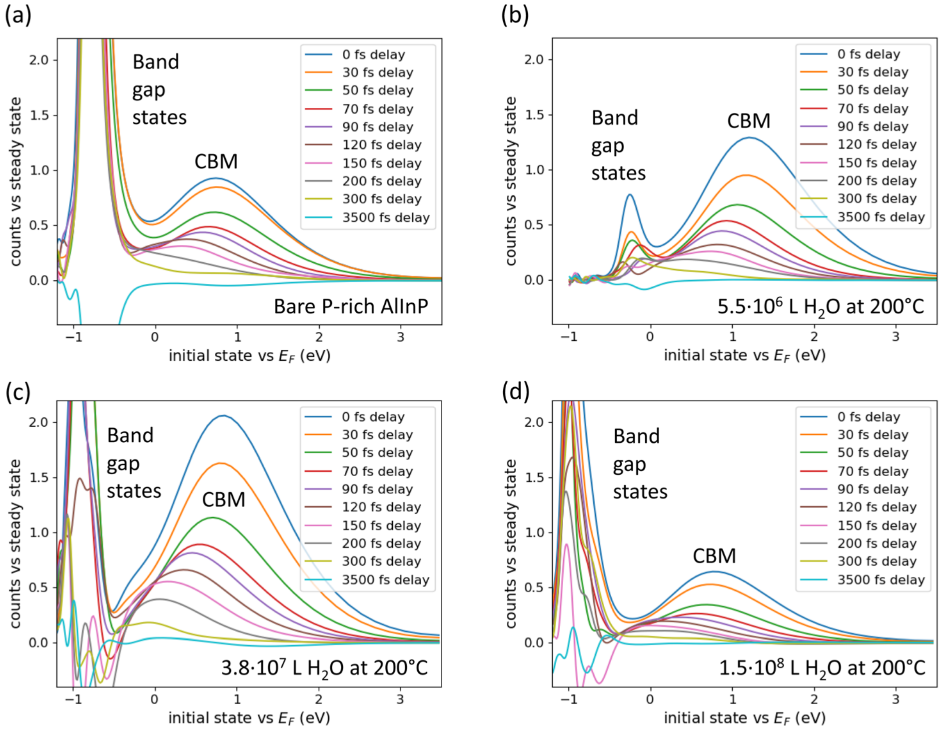

Fig. 7 Time-dependent component of photoemission from Fig. 6 for the bare P-rich AlInP surface (a), and after 5 (b), 30 (c), and 100 pulses (d) of water exposure at 200 °C. All panels share the same energy scale, showing that CBM emission intensities remain within about a factor of 3 between exposure levels, whereas sub-Fermi-level emissions change more markedly.

barrier to a surface dipole associated with the buckled P–P dimer reconstruction of the (2 × 2)-2D-2H AlInP (001) surface. Notably, the measured CBM position and the inferred valence-band maximum (VBM) on the bare surface are consistent with the UPS-derived band alignments, indicating that any changes to near-surface band bending are minimal. Table S4 (in SI) quantitatively tracks the evolution of the surface dipole, photoemission threshold, and state lifetimes with water exposure. In summary, before water exposure the tr-2PPE spectrum reflects a mid-gap-pinned Fermi level (due to surface states) and a slight intrinsic surface dipole that lowers the local vacuum level.

Initial water exposure (5 pulses, equal to 5.5×10^6 L) causes a pronounced upward shift of the low-energy cut-off by approximately +0.18 eV, indicating that the effective surface barrier has increased by this amount. This likely reflects the addition of a surface dipole that selectively inhibits the escape of the lowest-energy electrons. Importantly, the CBM peak remains nearly unchanged, shifting by only 0.15 eV to 1.20 eV after this initial dosing – demonstrating that the CB edge is largely unaffected by the surface modification. Consistently, the UPS work function (Φ) rises by ∼0.32 eV after the first water dose, in line with the 0.18 eV cut-off shift observed in tr-2PPE. Upon further water dosing, this trend reverses. After 30 pulses (3.8×10^7 L) at 200 °C, the low-energy cut-off shifts downward by 0.31 eV, and after 100 pulses (135 total, 1.5×10^8 L) it stabilizes at 0.13 eV below the original (pre-exposure) value. In other words, the initial barrier increase is not only undone but the surface barrier is slightly lowered compared to the pristine surface. Correspondingly, by 35 pulses the UPS-derived Φ returns to within experimental uncertainty of its initial value. These work function changes mirror the surface dipole evolution observed by tr-2PPE.

Throughout the later exposure stages, the CBM photoemission peak remains remarkably stable at 1.20 eV emission energy or about 0.85 eV *vs.* E_F for the initial states from which emission occurs (within experimental error). By contrast, UPS Φ changes (+0.32 eV) and VBM shift relative to the Fermi level (+0.24 eV) would suggest that the VBM and CBM should move down by around 0.56 eV *vs.* vacuum energy during initial oxidation, before recovering their initial position upon further exposure. However, the tr-2PPE CBM does not follow this prediction: on the bare surface it appears about 0.35 eV lower in energy than the UPS-inferred CBM position, and after the initial water dose it appears about 0.37 eV higher than expected, only converging with the UPS values at higher exposure levels. In other words, water- and heat-induced oxidation causes negligible real movement of the band edges relative to the detector. This discrepancy arises because UPS assumes a rigid shift of the band structure relative to the vacuum level, whereas tr-2PPE probes the photoemission threshold directly, which can shift due to surface dipoles without actually moving the semiconductor band edges. The evolution of the cut-off energy can be understood in terms of transient surface dipoles forming and dissipating during water exposure. Initially, the clean P-rich surface carries a built-in dipole on the order of hundreds of meV, likely originating from its polar P–P dimers (this intrinsic dipole is responsible for the 0.56 eV initial cut-off). Water dosing leads to rapid surface hydroxylation: XPS and UPS indicate the formation of Al–OH groups (see Fig. 5). These hydroxyl species likely orient with their negative end (O^- or OH^-) towards the surface, bonding to positively polarized Al atoms. DFT calculations, not shown here, reveal that OH adsorption leads to a reduction of Φ. The OH^- dipole partially screens the surface P–P dipole and reduces barriers to emission. However, after initial water exposure (5 pulses) we notice an increased Φ and suppressed low-kinetic-energy emission (Fig. 6). This may be related to transient surface rearrangements or other changes not fully captured in the DFT calculations preformed, initially increasing natural dipole barriers.

As water exposure continues, the surface chemistry evolves from this hydroxylated state toward a more fully oxidized surface, and the net dipole at the interface relaxes. The XPS/UPS data show that the initially abundant Al–OH species are gradually consumed or incorporated into an oxide network: Al–OH signals diminish while new Al–O–Al and In–O–P oxide species grow, and the P–P dimer structure is disrupted or oxidized. The formation of this oxide layer (likely an amorphous mixed Al/In oxy-phosphate) reduces the overall surface dipole compared to both the pristine dimer surface and the intermediate OH^- covered surface. An oxidized surface tends to have its charges more symmetrically distributed or internally compensated, yielding a smaller net dipole at the interface. Additionally, eliminating some of the P–P dimers and removing polar adsorbates removes part of the original dipole contributions. The net effect is that the initial dipole field is neutralized or slightly overcompensated as water exposure increases. This explains the downward overcorrection (the cut-off ending 0.13 eV below its initial position) of the cut-off: by the final exposure stages, low-energy electrons can escape more easily than on the clean surface because the surface barrier is lower than it originally was. In summary, the rising and falling of the photoemission threshold is a direct manifestation of forming and relaxing interfacial dipoles: initial water adsorption increases the P–P dimers natural dipole initially, raising the local vacuum level, and continued exposure/oxidation dissipates that dipole, lowering the vacuum level below its initial value. Importantly, these significant vacuum-level changes occur without any substantial movement of the semiconductor band edges, as discussed above.

These findings are in good agreement with theoretical expectations: the CB states of AlInP are calculated to be largely unaffected by molecular water and only slightly perturbed by surface OH^- groups. The resilience of the CBM is remarkable given that it lies within a 2–7 nm photoelectron escape depth, so very close to the surface, and is likely crucial for interfacial charge transfer, yet remains essentially unperturbed by changes in the topmost atomic layers. The combined tr-2PPE andXPS/UPS data thus paint a nuanced picture: surface chemical reactions initially affect local electrostatic dipoles but soon reach a steady-state where the band edges remain at their original positions throughout. The stability of the CBM, alongside the transient nature of any dipole-induced barriers, helps explain the excellent performance of AlInP as a window layer in III–V heterostructures. The CBM feature's intensity likewise remains within the same order of magnitude across all exposure stages, indicating that these near-band-edge states are neither eliminated by oxidation nor heavily depopulated. In our measurements the CBM peak amplitude varied by at most a factor of three between the pristine and most oxidized surfaces. Only a slight downward trend in CBM signal is observed at the highest exposures, which we attribute to the growing oxide layer attenuating photoelectron escape rates. Importantly, there is no evidence of any drastic quenching of the CBM emission; the key near-surface CB states persist robustly through the surface changes.

It is notable that the ultrafast decay dynamics of the CBM feature remain largely unchanged. On the pristine P-rich surface, electrons excited into the near-surface CBM decay with a characteristic lifetime of ~90 fs (Fig. S11 and S12(a) in the SI). After the initial water exposure, the CBM decay becomes only slightly faster (~80 fs, Fig. S12(b and c) in the SI), and by the final heavily oxidized stage it is ~70 fs (Fig. S12(d)). This modest ~20 fs lifetime reduction suggests a slight increase in available relaxation pathways in the presence of the oxide, for instance, *via* defect states in the nascent oxide that provide additional scattering channels. The CBM state remains an ultrafast-decaying state in all cases, and we do not observe any order-of-magnitude change in its lifetime. The persistence of a short CBM lifetime and stable CBM energy despite extensive surface hydroxylation/oxidation strongly indicates that the CBM-related photoemission originates from a near-surface (or sub-surface) resonance of the AlInP conduction band, rather than from a state localized at the very surface. If the CBM peak were due to a surface-localized state (for example, a state tied to the P–P dimers or a shallow surface quantum-well), one would expect its energy or lifetime to change dramatically upon altering the surface chemistry. Surface-localized states are extremely sensitive to bonding and atomic coordination at the surface, so significant hydroxylation and oxide formation would likely shift their energy or even quench them entirely. In contrast, the observed near-constant CBM energy and only slight lifetime shortening imply that this feature is predominantly governed by the bulk-like electronic structure of AlInP just beneath the surface, and is only weakly affected by modifications in the outermost layers. This is in agreement with DFT calculations (Fig. S7 in the SI), where the CBM is dominated by bulk states at Γ which remain stable under the calculated adsorbates. This resilience is remarkable given that the CBM lies within a 2–7 nm photoelectron escape depth,[73] very close to the surface and likely to play a key role in interfacial charge transfer, yet remains unaffected by changes in the topmost layer. In practical terms, the CBM resonance behaves as if it were "buried" a few atomic layers deep: tr-2PPE can still detect it (given the few-nanometer escape depth of photoelectrons), but the state's character is bulk-like enough that surface perturbations do not appreciably shift it.

Meanwhile, the mid-gap emission (from states at or just below E_F) continues to dominate the low-energy portion of the spectra (see Fig. 6) even after water exposure. This behavior is expected in tr-2PPE, since electrons in mid-gap surface states can be emitted by the 4.49 eV probe photon alone, requiring no pump excitation, whereas CBM emission necessitates an initial pump to populate the state, inherently limiting its intensity. The persistence of this strong sub-gap emission confirms that the Fermi level remains pinned by surface/interface states throughout the exposure sequence, despite the changing surface chemistry. We also observe that the effective lifetime of electrons near E_F increases from ~70 fs on the bare surface to ~170 fs at the highest exposure, more than doubling as the surface becomes oxidized. In other words, once the surface is modified by hydroxylation and oxide growth, electrons in the mid-gap states recombine more slowly. This suggests that the oxidized interface introduces fewer ultrafast nonradiative pathways for those electrons, or oxide-related defect states may act as shallow traps that slow their decay. Thus, while the mid-gap states pinning E_F persist through the entire water exposure sequence, the presence of surface hydroxides/oxides extends their lifetimes, causing electrons to remain trapped in these states for longer. We note that immediately after the initial water exposure the time-resolved signal near E_F was noisy, precluding a reliable fit for that stage; however, the overall trend of increasing lifetimes with increasing oxidation is clear for the subsequent steps. Taken together, the tr-2PPE results reveal that surface dipole barriers evolve markedly with initial water exposure and then diminish upon oxide formation, while the CBM position and lifetimes remain spectroscopically and dynamically stable. The combined tr-2PPE and XPS/UPS findings suggest that surface reactions initially affect local electrostatic dipoles but soon reach a steady state where the CB edges are unchanged. This is likely to be a key reason why AlInP performs well as a window layer; even if AlInP undergoes environmental exposure and oxidation, its critical CB edge stays fixed, preserving favorable band alignment for charge transport, and any introduced interfacial barriers are low in energy and short-lived.

Finally, we compare these results with the P-rich InP (001) surface under similar conditions. P-rich InP shares the same dimerized P–P surface reconstruction as AlInP but contains no Al. In previous experiments by some of the present authors,[72] P-rich InP subjected to identical water dosing (also at 200 °C) showed minimal work function changes with no significant low-energy cut-off shift, so no appreciable dipole-induced vacuum level shift was observed. Instead, water increased the surface CBM-state lifetime by at least an order of magnitude.[71] This dramatic slowing of electron decay on InP was attributed using DFT to adsorbed H_2O and the formation of surface indium phosphate species that damp high-frequency surface vibrational modes, thereby reducing nonradiative recombination. By contrast, P-rich AlInP shows a surface dipole after initial water exposure, not observed on InP, while its CBM-related state retains an ultrafast decay even after significant oxidation. The mid-gap Fermi-level pinning state on AlInP does become longer-lived upon hydroxylation and oxidation, but is still an order of magnitude shorter lived than on InP, where CBM and Fermi level lifetimes are in the picosecond range.[71] This suggests that the AlInP surface hosts fewer or different trap states than InP even in the pristine state. More broadly, substituting Al fundamentally changes the surface response. The bare P-rich AlInP surface does not exhibit the multitude of CB surface states that InP does, where six CB-related resonances were observed on InP under the same tr-2PPE conditions,[71] as shown in Fig. 8. Moreover, water- and heat exposure on AlInP produces primarily Al–OH and oxide species with negligible phosphate formation. Crucially, AlInP maintains a stable near-surface CBM energy and reverts to a low-dipole state after the initial modification. Thus, a P-rich AlInP window layer can withstand water exposure or oxidation while retaining its band-edge alignment. This interfacial stability under conditions representing adlayer deposition or electrolyte exposure reinforces the status of AlInP as a state-of-the-art III–V window layer.

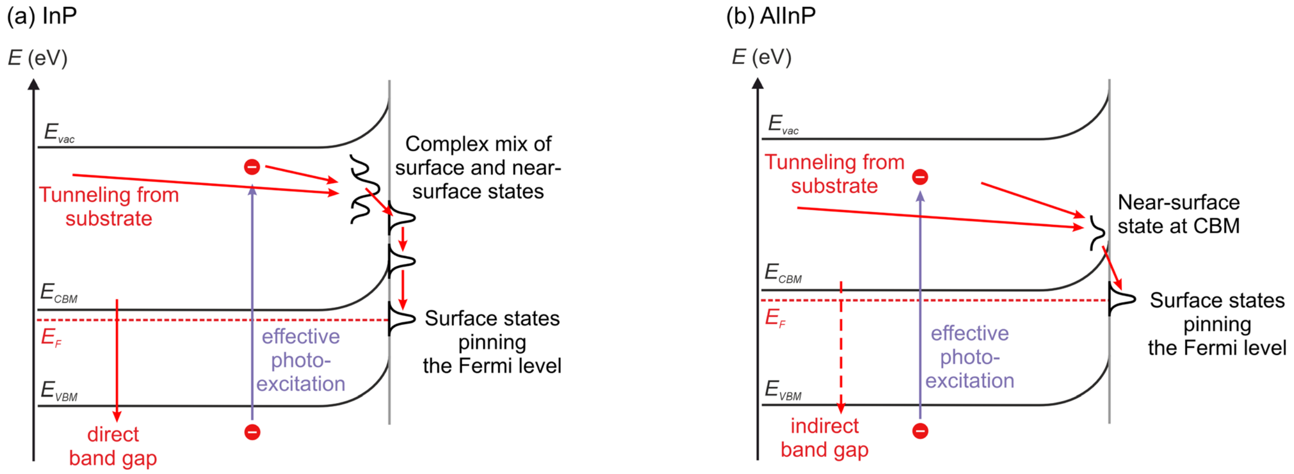

Fig. 8 Schematic of photoexcitation in InP (a) and AlInP (b), interpretation based on ref. 71 for InP, and ref. 16 as well as the present work for AlInP. In InP, a complex mix of surface and near-surface CB states is found. The substitution of some In for Al in AlInP leads to only a single near-surface state at the CBM. This state is much more resilient to surface modification than the complex InP CB structure, which is modified by water- and heat exposure, and was easily passivated by oxygen exposure during measurements in ref. 71 and 72 by the present authors, not the case for AlInP, though this comparison was not measured in detail.

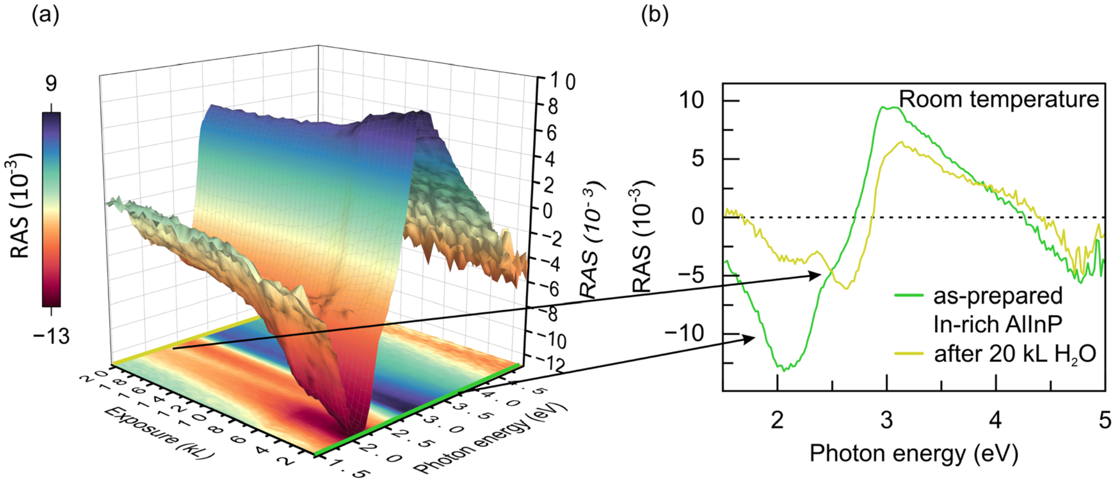

Fig. 9 (a) 3D color plot of *in situ* RAS measurement during exposure of 20 kL of water to In-rich AlInP (001) surface and (b) RA spectra measured at the beginning and end of the exposure. Green spectrum: as-prepared In-rich AlInP; olive spectrum: after 20 kL water exposure.

2.2 Oxidation processes on the In-rich AlInP (001) surface and their impact on electronic and chemical structure

The modification of In-rich AlInP *via* oxidation using water and oxygen was investigated to understand the influence of AlInP surface reconstruction on its surface reactivity (modification of the surface upon exposure to air is discussed in Fig. S14 in the SI). The interaction of an In-rich AlInP surface with water gas in vacuum is investigated using a methodology analogous to that described in the previous section for the P-rich surface. The In-rich AlInP surface was prepared and characterized as described in ref. 16. The prepared sample was then exposed to water, with *in situ* monitoring of surface changes using RAS. Fig. 9(a) presents the 3D color plot from the *in situ* measurement, and (b) shows the RA spectra corresponding to the initial and final measurements, extracted from the color plot.

The first spectrum (green) is identical to the RA spectrum of the In-rich AlInP surface after preparation as reported in ref. 16, confirming that the surface of the sample is free of contamination and the (2 × 4)-rInMD surface reconstruction. The first monolayer of the (2 × 4)-rInMD consists of In–P mixed dimers, while the second monolayer illustrates the existence of In–In dimers[16] (top view in Fig. 11(a); will be discussed in the following). The pronounced negative peak at 2.1 eV on the pristine surface is associated with transitions involving the In–In bonds located in the second layer beneath the surface.[16] Significant alterations in the spectral line shape occur following a 20 kL exposure to water. Notably, this negative peak observed in the RA spectrum decreases within the initial 10 kL of water exposure and subsequently remains constant. The intensity of the peak at 3.0 eV decreases only slightly, and remains stable after 10 kL. Analogous to the response of the RA spectra of P-rich samples upon water exposure, a blue shift is also observed here, particularly pronounced at lower photon energies. Due to the stabilization of the RA spectra, the exposure was stopped, and the sample was transferred to the analysis chamber.

The green and olive spectra in Fig. 10 show XP spectra of In-rich AlInP measured at 15°before and after exposure to 20 kL water, respectively. Initially, no C or O contamination was detected on the sample, confirming the cleanliness of the UHV transfer process (see Fig. S4(b) in the SI). Notably, even after exposure to water, C contamination remains absent. Upon exposure to 20 kL of water, the evolution of emissions within the O 1s region is observed.

Examining the core levels of AlInP reveals that in contrast to the P-rich surface – where the Al 2p core level is the first to exhibit changes upon exposure, indicating a high reactivity of the Al sites to water molecules – alterations in the In 3d spectral line are observed. The emission at 444.0 eV decreases in the In $3d_{5/2}$, indicating that In–In bonds on the In-rich surface are dissociated upon exposure to water. Considering the asymmetric increase at higher BEs of In $3d_{5/2}$ (visible in the difference spectrum), this observation suggests the formation of In–OH and In–O–P bonds. Considering that the emission peak is located at 445.20 eV, it is probable that the concentration of In–OH bonds is larger than In–O–P bonds. Although the P 2p line in XPS demonstrates low sensitivity, the absence of emissions within the 133–136 eV range may indicate that the formation of In–OH bonds dominates over In–O–P bonds. The formation of a trace of In–O–In bonds on the In-rich surface upon exposure is anticipated because the emission of the O 1s line ranges from 529.20 to 535.00 eV (indicated with a red arrow in O 1s). Hence, two emission lines at 530.00 and 532.70 eV, each with a FWHM of 1.8 eV, can be considered here, corresponding to In–O–In bonds.

Fig. 10(c) presents the UP spectra of VB before (green) and after exposure (olive and orange) experiments utilizing He I excitation. The UP spectrum undergoes significant alteration following exposure to 20 kL of water (olive). Upon examining the difference spectra, there is an evident attenuation of the signal up to 4.50 eV, implying a partial elimination of surface states of AlInP. Another factor contributing to the observed downward signal in the difference spectra is the predominance of

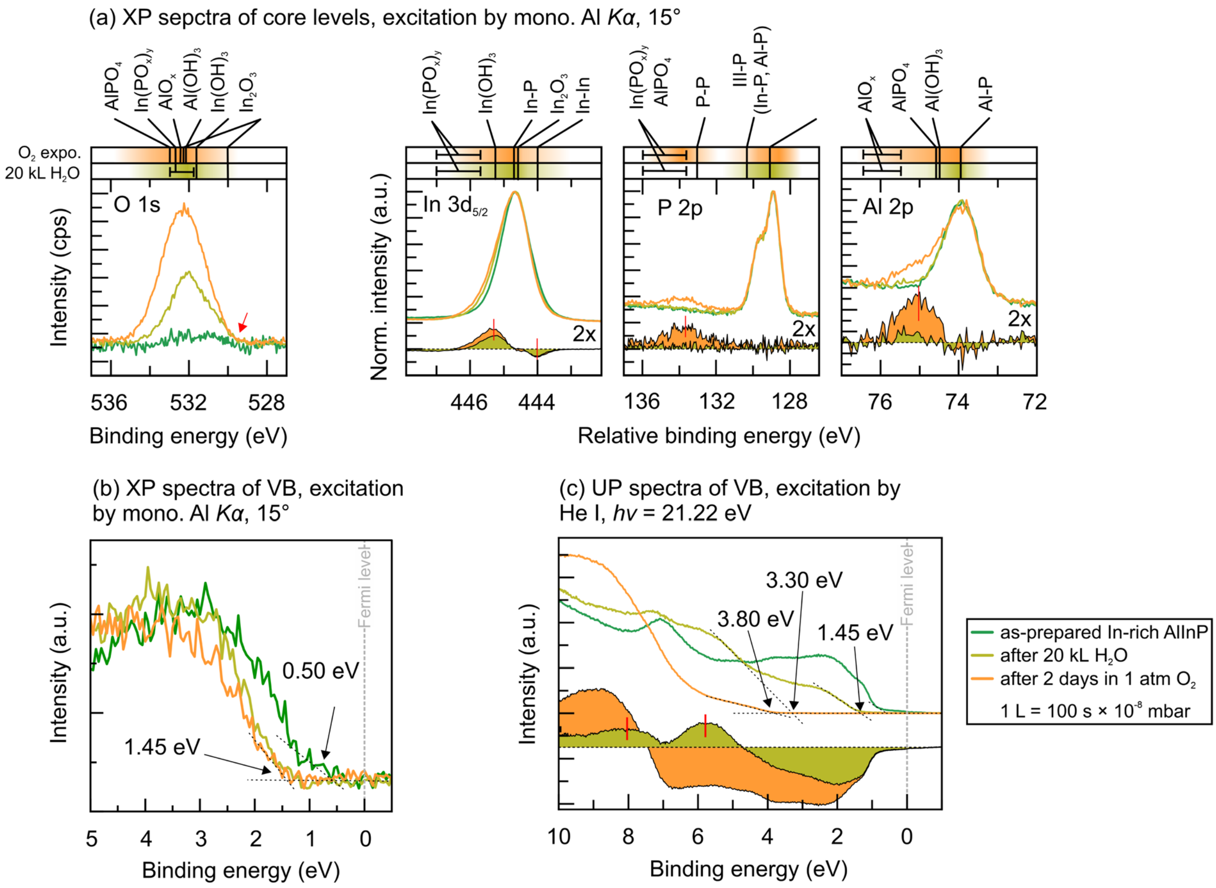

Fig. 10 (a) HR XP spectra of O 1s, In 3d$_{5/2}$, P 2p, and Al 2p core levels (left to right) for In-rich AlInP (001), recorded before (green) and after exposure to 20 kL of water (olive), and 2 days storing in 1 atm O_2 (orange). To demonstrate the spectral changes induced by exposure, In 3d$_{5/2}$, P 2p, and Al 2p core levels spectra are normalized to their respective maximum intensity, and the post-exposure spectra are shifted to maximize overlap with the as-prepared spectra. Accordingly, the *x*-axis is labeled as "relative binding energy." Difference spectra *vs.* In-rich are multiplied to two and plotted. The horizontal bars positioned above each spectrum specify the BE ranges of various oxide species, serving as references to facilitate peak assignment. (b) The XP and (c) UP (He I excitation) VB spectra of In-rich AlInP before and after exposure.

emissions from surface oxides/hydroxides formed, which hinder the emission originating from the underlying AlInP layer. Given that the oxide layer's thickness is considerably smaller than the IMFP of electrons when excited by He I radiation, the AlInP VB located beneath the oxides remains detectable even after 20 kL water exposure. Consequently, the signal in the 1.45–3.8 eV range is attributed to the AlInP VB. Evolution of the emission near approximately 6 and 8 eV (indicated by red lines in Fig. 10(c)) closely resembles the findings regarding the interaction of water with the P-rich surface (see previous section, Fig. 2 and 5). Since these VB features are associated with OH^- groups,[34,37,67,68] the results suggest the formation of In–OH during the initial 20 kL water exposure. This inference is supported by the emission lines of O 1s and In 3d$_{5/2}$, as illustrated in Fig. 10, olive spectra. As no alterations are evident in Al 2p after 20 kL water exposure (olive spectrum), the presence of Al–OH is likely negligible, if present at all.

Water exposure effects on the In-rich (2 × 4)-rInMD AlInP are evaluated by comparing them with the oxidation characteristics of In-rich (2 × 4)-InMD InP,[31,32,35] given that the atomic species and relative positions between the surface reconstructions are almost identical, as outlined in ref. 16. It was demonstrated that individual adsorbed water molecules preferentially bond with In surface atoms.[31] It was revealed that dissociative adsorption is thermodynamically more favorable than molecular adsorption. When dissociation occurs, the hydroxyl group preferentially bonds with In–In dimers, while hydrogen atoms are more likely to adsorb onto the mixed-dimer P atom. This observation aligns with the experimental results regarding water exposure on In-rich (2 × 4)-rInMD AlInP found in this study. Cleaved gallium arsenide (GaAs) (001) surfaces undergo hydroxylation, which facilitates the adsorption of water molecules by forming hydrogen bonds with surface OH^- species.[59] Additionally, the hydroxyl group demonstrated stability on the surface even at temperatures up to 946 °C (673 K).[59] Moreover, it has been suggested that a similar interaction mechanism takes place between water and a cation-rich InP surface. In this scenario, water films on InP are stabilized through anchorage to hydroxyl groups bonded to the surface.[31] Therefore, upon comparing these findings with the literature,[35] it appears that the presence of Al in the fourth monolayer beneath the surface modifies the

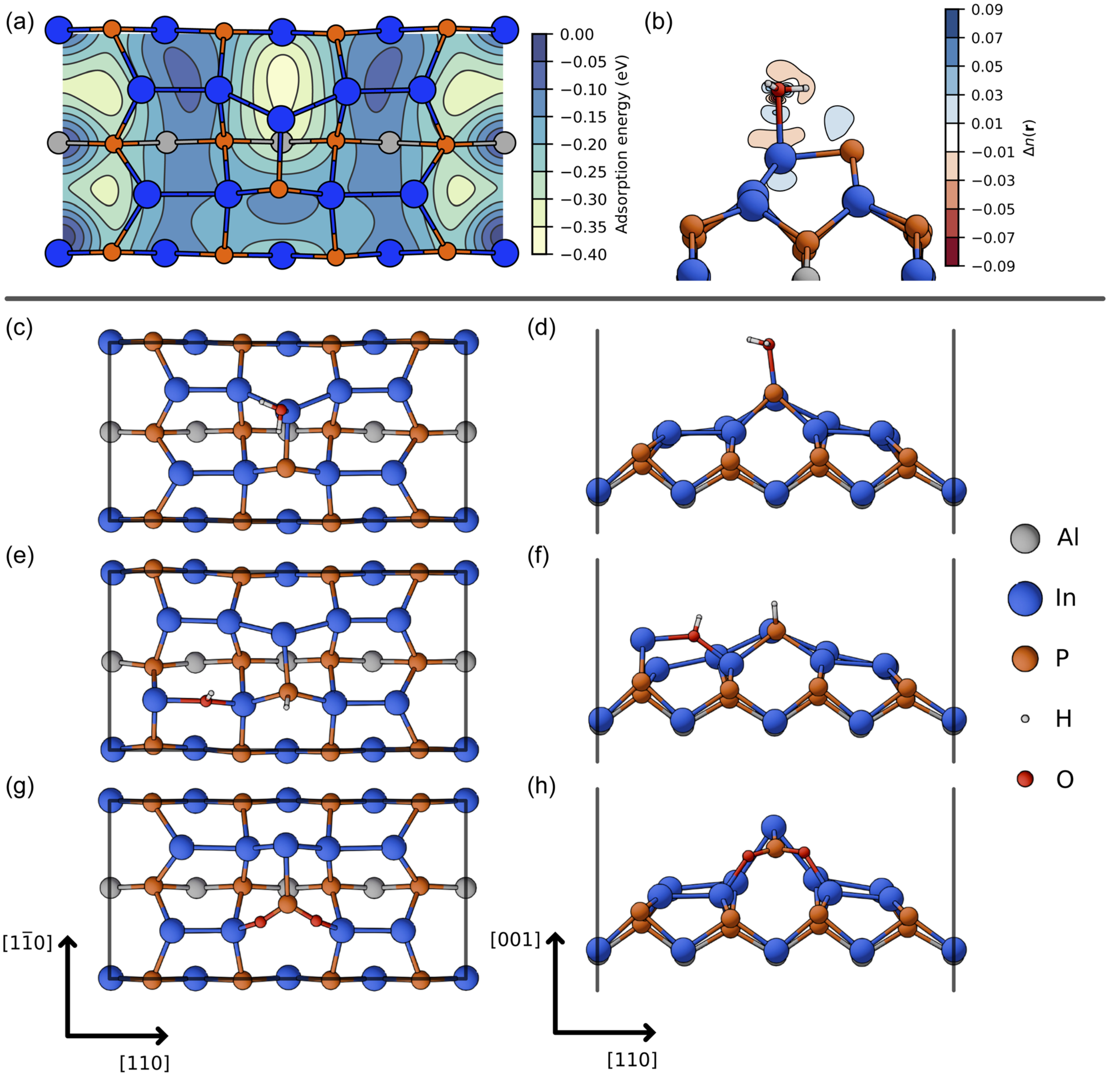

Fig. 11 Calculated potential energy surfaces for single water molecules on In-rich AlInP (001) (2 × 4)-rInMD (a). A more negative adsorption energy indicates a more favorable adsorption site. Calculated water-induced charge redistribution for water adsorbed on the top mixed dimer of the (2 × 4)-rInMD (b), blue and red isosurfaces signify areas of charge accumulation and depletion, respectively. Top (c) and side (d) view of the most energetically favorable structural configuration for a single adsorbed water molecule on the top mixed dimer. Top (e) and side (f) view of the most energetically favorable structural configuration for an adsorbed OH group. Top (g) and side (h) view of the most energetically favorable structural configuration for adsorbed two O atoms.

surface chemistry, enhancing the likelihood of hydroxyl group formation and possibly also forming Al–OH bonds.

To validate the experimental findings, DFT calculations were employed to determine the configuration of water adsorption on the (2 × 4)-rInMD surface. The potential energy surface, which describes the adsorption of a single water molecule on the AlInP (001) (2 × 4)-rInMD surface, is illustrated in Fig. 11(a). Full relaxation calculations for the water molecule showed that the adsorption energy is essentially identical between adsorption on the dangling bonds of the second row In atoms or at the top In dangling bond, despite the different chemical environment. The adsorption energy is calculated to be −0.40 eV for both sites. Fig. 11(c) and (d) illustrate the top and side views of the structural arrangement of molecular water when adsorbed on the surface top mixed dimer. For this AlInP surface, it is particularly surprising that there is a preference for the topmost In atom compared to the three-fold coordinated In atoms of the second row, in contrast to the adsorption found for the In-rich InP surface, despite both surfaces having the same chemical composition for the first 3 layers.[31] The difference in size of the

Al atoms compared to the In atoms might explain the different bonding scenarios. This is evident in the AlInP lattice constant being smaller than that of InP, resulting in slightly smaller bond lengths in the AlInP surface, which in turn will equivalently change the electronic environment, explaining the adsorption differences between the AlInP and InP surfaces. Molecular adsorption on the second-row In atoms is found in the same configuration as for the In-rich InP,[31] *i.e.*, forming an In–O bond with the H pointing downwards (see Fig. S6(a) and (b)).

Fig. 11(b) illustrates the equilibrium bonding configuration of a water molecule adsorbed onto the top In–P dimer of the surface, along with the computed charge redistribution induced by this adsorption. There is a charge accumulation between the water's O and the In atom in the first monolayer. The $1b_1$ orbital of the water molecule donates electrons to the dangling In p-orbital. A minor interaction between one of the hydrogen atoms and the P atom is observed, with the O–H bond oriented parallel to the In–P bond. For the water molecule adsorbed at second-row In back-bonds (Fig. S6(c)) the charge redistributes in a similar manner to the one found for the In-rich InP surface.[31] Electronic structure calculations reveal that water adsorption does not contribute any additional states within the band gap (*cf.* Fig. S15(a–c)), furthermore the band gap size remains the same. There is a small modification of the conduction states near the band gap. The effect is more pronounced for a water molecule adsorbing at the second-row In back-bonds, notably, the unoccupied state C2 is pushed downwards in energy (see Fig. S15(c)).

Similar to the P-rich surface, AIMD calculations were performed for the water/AlInP interface of the (2 × 4)-rInMD surface at 350 K (see Note S1 in the SI). The first hydration layer forms remarkably close to the surface bonding to the under-coordianted In atoms of the second layer as can be seen from the density profile (Fig. S8(d) in the SI). The water molecules are orientated on average in an H-down configuration, similar to the one found for single molecular adsorption at 0 K. The second hydration layer adopts an O-down orientation consistent with bulk-like water structuring and electrostatic layering effects. Additionally, some water molecules adsorb with a sideways orientation on top of the mixed dimer not captured in Fig. S8(d), but can be seen in Fig. S8(c). This is a similar orientation observed for single molecular adsorption on the top In atom. No water dissociation was observed during the 20 ps AIMD timescale, the observed proximity of water to surface In atoms and the orientational bias together indicate a reactive interfacial environment, one that may facilitate proton transfer and hydroxylation over longer timescales.

Following water molecular adsorption, water dissociation is studied by investigating the adsorption of hydroxyl species on the surface. The adsorption energies were calculated using eqn (2) (see Section 4) and $E_\mathrm{A} = E_{\mathrm{H_2O}}$, considering hydrogen also adsorbs at the surface. The most energetically favorable configuration, with an energy of −0.31 eV, is shown in Fig. 11(e) and (f). The OH adsorbs preferentially between an In–In bond of the second row and the H at the top P dangling bond. As a result, the surface geometry is a modified form of the relaxed ground state, this is more evident on the three-fold coordinated In atom which is lifted upwards. This adsorption configuration on the AlInP In-rich surface is similar to the one found for InP surface.[31] However, in the case of AlInP, the adsorption energy is lower for the intact water compared to the OH and H adsorption, *i.e.*, molecular adsorption is favored. Additionally, similar energy barriers found for the InP[28,31] surface might be present for the AlInP surface, further hindering water dissociation. Despite this, once the full water/surface interface is taken into account water dissociation may be energetically preferred. On the (2 × 4) InP surface water layer formation is observed to anchor onto hydroxyl groups present at the surface, enhancing dissociative adsorption.[31] The electronic structure of the OH adsorbed at the AlInP surface (Fig. S15 in the SI) reveals that while the band gap remains essentially the same, there is a stronger effect on both occupied and unoccupied states close to the band gap compared to the other types of adsorption studied here. In particular the dispersion for the highest occupied band is reduced, and the second lowest unoccupied state C2 is further pushed down in energy. This is not surprising as the states near the band gap are related to the In–In bonds of the second layer.[16] Thus, dissociative water adsorption on the second In atoms results in modification in the electronic states related to the negative feature of the RAS signal around 2 eV.[16] This can explain the dampening observed as exposure is increased (see Fig. 9). Similarly to a molecular adsorption, there are no additional states introduced in the band gap that could affect the BB.

In the next step, oxidation on the In-rich AlInP surface was explored. An energetically favorable configuration for two adsorbed O atoms is shown in Fig. 11(g) and (h). Here, each O atom adsorbs at the In–P bonds between the top dimer and second row, in mirroring positions, forming In–O–P bonds. The inserted O atoms push the top mixed dimer in the [001] and $[1\bar{1}0]$ directions. In addition there is a small rearrangement of the In atoms in the second row. It is important to note that O adsorption was only found to be energetically favorable when two O atoms were considered. The energy adsorption per adsorbate for this configuration is −8.2 meV calculated with the following equation

$$E_\mathrm{Ads} = (E_\mathrm{A+surf} - E_\mathrm{surf})/2 - E_\mathrm{A} \qquad (1)$$

with $E_\mathrm{A} = E_{\mathrm{H_2O}} - E_{\mathrm{H_2}}$. This geometry has been previously proposed and studied for the In-rich InP surface.[31,32,35] It is, however, less favorable than the molecular and dissociative water adsorption discussed above. Although, the adsorption energy per molecule could potentially decrease when the entire water–surface interface is considered. Adsorbed O or OH ions at the surface could serve as anchor points for the water layers that form on top. This phenomenon has been observed previously on the InP surface, see ref. 31 and 59. Yet, the less favorable adsorption explains why XPS results suggest a larger concentration of In–OH bonds compared to In–O–P bonds. Furthermore, dissociative adsorption on the already adsorbed hydroxyl groups could lead directly to In–O–In even though they are found here not to be favorable. This could be a result of rather high diffusion barriers but further studies are needed in order to fully comprehend the dissociation process. The electronic structure (see Fig. S15(e)) reveals a strong effect on the occupied and unoccupied states close to the band gap. This is a result of the relaxation of the top two rows which in turn affects the surface states energetics. This would coincide with a further decrease in the RAS signal strength in Fig. 9.

The DFT calculations show that the adsorption of water molecules on the In-rich surface is favored over adsorption on the P-rich surface, exhibiting approximately twice the adsorption energy. The presence of Al atoms appears to have a negligible influence as they are only present in the fourth layer and below. These observations align with experimental interpretations, suggesting that In atoms primarily interact with water which leads to the dissociation of In–In bonds, whereas the Al does not show a significant influence on the interaction with water. The full dissociation reaction mechanism have not yet been included in DFT calculations; however, the initial calculations performed offer an understanding of the most energetically favorable adsorption sites for water and OH molecules as well as atomic O, which is consistent with experimental findings. The dissociation process is proposed to follow water molecules adsorbing at the top mixed dimer. Soon thereafter one of the hydrogen bond breaks adsorbing the H on the top P dangling bond and the OH^- at the second layer In–In bonds. The similarities between these findings and those obtained from analogous surfaces may contribute to a first approximation about the dissociation mechanism on AlInP surfaces, *i.e.*, the reaction paths and transition states. Furthermore, this study may be extended to other III–V semiconductors, in particular those with similar surface reconstruction, by helping to identify surface-active sites and possible water dissociation paths.

The exposure experiment was prolonged by placing the water exposed sample in an oxygen-filled chamber at 1 atm for two days. Subsequent XPS analysis was performed to examine the chemical alterations. The orange spectra in Fig. 10(a and b) illustrate the XPS results. An enhanced intensity of the O 1s emission line signifies an elevated concentration of oxides present on the surface. Analysis of the difference spectra reveals no further reduction at 444.00 eV in In $3d_{5/2}$, implying that the majority of In–In bonds have already been dissociated after exposure to 20 kL of water. Notably, there is a further increment around 445.20 eV, associated with the rising presence of In–O–P. The formation of In–O–P is supported by the evolution of an emission within the 132–136 eV range. Simultaneously, alterations in the Al core level suggest the formation of Al–O–Al and Al–O–P.

The UP spectrum, following the storage of the sample in O_2, reflected in the orange spectrum of Fig. 10(c). The thickness of the oxide/hydroxide layer grows further with the oxidation of the In-rich surface. As the oxide layer surpasses 3 × IMFP of electrons in UPS, the AlInP layer beneath the oxides becomes undetectable by UPS. The VBM of the oxides increases from 3.30 eV after 20 kL water exposure to 3.80 eV following prolonged O_2 exposure. The rise in VBM induced by further oxidation is consistent with the observations on the P-rich AlInP surface. The VBM of AlInP beneath the oxides as measured by XPS (Fig. 10(c), orange spectrum) is 1.45 eV. Furthermore, the VB features related to hydroxyl groups are no longer detected. Hence, extended O_2 exposure leads to the dehydrogenation of hydroxyl species and further oxidation on the surface.

The band diagrams of modified In-rich AlInP surfaces following sequential exposures are presented in Fig. 12. Fig. 12(a) shows the band alignment of an as-prepared In-rich surface, (b) shows an In-rich surface after exposure to 20 kL of

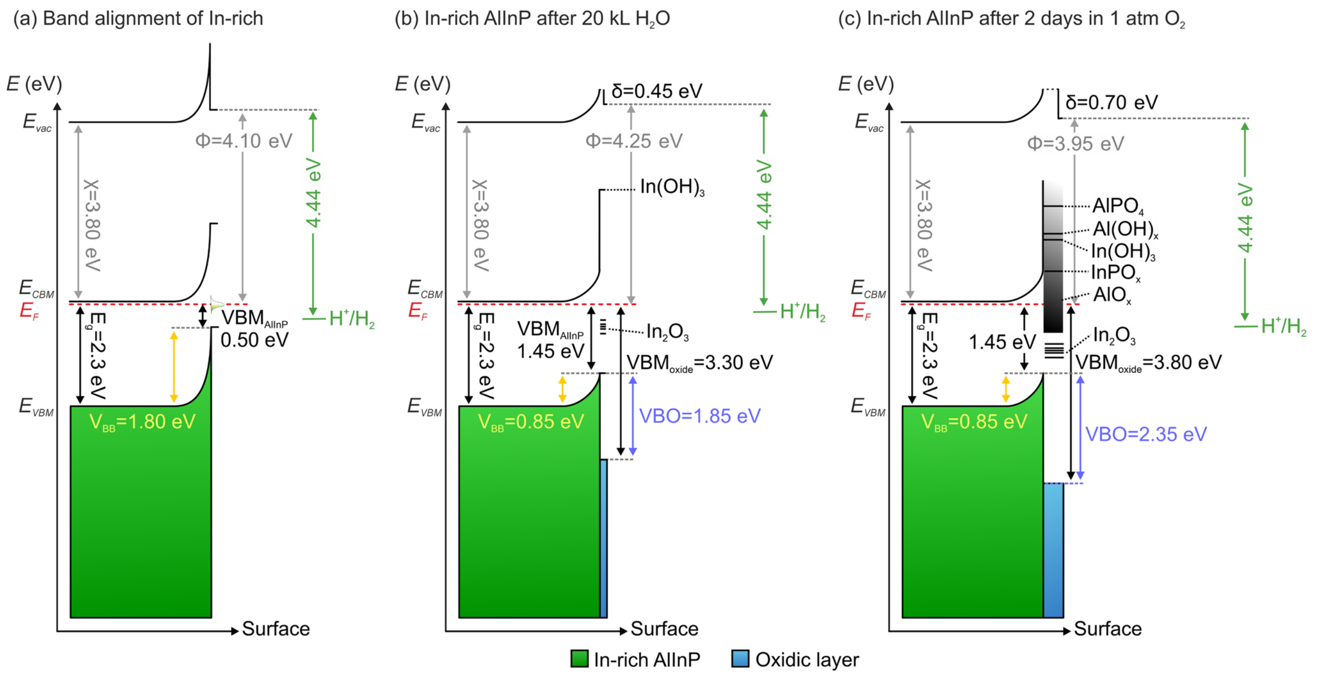

Fig. 12 The band alignment of In-rich AlInP before (a), and after 20 kL water (b), and after long (2 days in 1 atm) O_2 exposure (c).

water, while (c) displays the further modifications after an additional two days in 1 atm of O_2. The diagrams are based on combined XPS and UPS analyses, which identify the specific oxides and hydroxides formed after each step. Band alignments were constructed by considering these chemical assignments together with the band gap of the most relevant compounds. After 20 kL, mostly In–O–In and In–OH are discernible; thus, the CBM for these two components is shown in Fig. 12(b). Subsequent oxidation of the surface through prolonged O_2 exposure leads to more complex surface chemistry. Consequently, multiple oxides are considered for the band alignment depicted in Fig. 12(c).

In Fig. 10, for constructing difference spectra, the peaks were shifted in BE. Therefore, detailed values of the core level peak maxima before and after exposure, measured at emission angles of 90° and 15°, are summarized separately in Table S5 in the SI. Across all core levels, a consistent shift of approximately 350 meV toward higher BEs is observed. Notably, the VBM position of AlInP exhibits a larger shift, increasing from 0.50 eV to 1.45 eV. As all observed shifts occur towards higher BEs, this implies an alteration and reduction in the magnitude of the BB. However, a more pronounced shift of the VBM indicates a modification in both the chemical composition and the surface characteristics of the AlInP.

As discussed in ref. 16, one key origin of Fermi level pinning at the In-rich AlInP surface is the formation of 1D In–In atomic chains in (2 × 2)-InMD-2H in minority domains, which introduce midgap states. Given the high reactivity of In–In sites toward water, the initial modifications upon exposure are attributed to dissociation of In–In dimers of (2 × 4)-rInMD and 1D In–In atomic chains in (2 × 2)-InMD-2H, leading to formation of In–O–In and In–O–P as well as a reduction in the surface BB. Remarkably, the ultimate position of the VBM in the AlInP layer beneath the oxide layer reaches 1.45 eV, which is similar to the observed value for P-rich surfaces following exposure. This finding indicates that only the magnitude of the BB on the In-rich surface changes, while a BB remains present. It implies that prior to exposure, midgap states attributed to 1D In–In atomic chains were predominant in determining the electronic properties.[16] The exposure eliminates these states, thereby allowing different surface states to subsequently influence the band diagram. Given that the VBM attains 1.45 eV on both surfaces, one reasonable explanation is the presence of a small concentration of P–P dimers with P dangling bonds on the In-rich surface that likely originates from growth process imperfections (effect of non-ideal preparation condition is discussed in ref. 16). These defects dominate the electronic structure by pinning the Fermi level on the surface of AlInP and inducing the BB in AlInP layer. Although the density of P dangling bonds is considerably lower compared to the P-rich surface, their presence may still introduce midgap states.

As previously discussed,[11,12,16] the role of AlInP as a charge-selective contact layer its due to its inherently high n-type doping, which significantly suppresses hole transport toward the surface. Consequently, midgap states introduced by surface oxidation or hydroxylation are unlikely to serve as dominant recombination centers under operational conditions. However, if the CBM of the surface oxide lies significantly above that of AlInP, it could introduce an energy barrier for electron transport, potentially affecting device performance. Therefore, identifying the chemical nature and electronic structure of the oxide species is critical. One of the differences in the oxidation behavior of In-rich and P-rich AlInP surfaces upon exposure to H_2O/O_2 is the formation of small concentration of In–O–In bonds on the In-rich surface. This bonding leads to a higher density of midgap states, which originate from III–O bonds and are known to act as electronic trap states, potentially reducing the functional quality of the oxide layer.[27,32] Nevertheless, considering the role of AlInP as a window layer – which inherently blocks hole transport due to both the large VBO at the AlInP/photoabsorber interface, and its high donor concentration, and small concentration of In–O–In–the probability of charge carrier recombination at these III–O midgap states remains minimal during operation.

3 Conclusion

We conducted a comparative study of P-rich and In-rich AlInP (001) surfaces, examining oxidation processes, surface chemical stability, and the composition of the resulting surface oxidic phases upon exposure to H_2O and O_2 under various conditions, depending on the surface reconstruction. The adsorption experiments primarily offered insights into the initial reaction steps. Surface reactivity was found to be determined by the distinct surface reconstructions. On the P-rich AlInP, characterized by P–P dimers on the topmost layer, a small amount of water rapidly altered the surface through partial elimination of surface states. Water molecules preferentially adsorb on Al atoms located in the second or third monolayer, while P–P dimers exhibit limited interaction with water. Observations indicate that water dissociates upon contact with this surface, leading to the formation of hydroxyl groups (Al–OH and In–OH) and Al–O–Al bonds. At higher exposures, additional oxidation and partial P–P disruption occur, but the near-surface band energetics remain robust. Even after prolonged exposure (from 314 kL to 1.5×10^3 kL), the VBM of AlInP beneath the oxidic layer remained at 1.45 eV, indicating the presence of surface states that continue to pin the Fermi level. Exposure results in an increase in the VBO at the oxide/AlInP interface, rising from 2.00 eV after 75 kL to 2.60 eV after 1.5×10^3 kL of water. Tr-2PPE showed a remarkable stability of near-surface CBM states to surface modification when compared to similar P-rich InP surfaces. While the photoemission threshold/work-function changes with transient dipole formation during initial hydroxylation, the near-surface CBM remains essentially fixed in energy and retains ultrafast decay dynamics across oxidation levels, supporting predictable band-edge alignment under interface modification. The stability of the CBM energy and -lifetimes under this modification helps explain the high performance of AlInP as a window layer, maintaining predictable band positions even under changes to the surface/interface.

In contrast, In-rich AlInP surfaces exhibited more extended surface modifications when exposed to water, interacting more rapidly than the P-rich surface. On the In-rich surface, the presence of In–In bonds in the outermost layers (second layer from top) altered the chemical behavior and increased the surface's chemical reactivity. Consequently, In atoms are more susceptible to changes compared to P and Al atoms, which are exclusively incorporated into III–P bonds (In–P or Al–P). In–In bonds exhibited higher reactivity than III–P bonds, and dissociate after only 20 kL water exposure. Additionally, hydroxylation also occurred on this surface. Extended O_2 exposure led to the dehydrogenation of hydroxyl groups, resulting in the formation of various oxides, notably In–O–P and Al–O–Al. Similar to the P-rich surface, upon oxidation, the VBM of the underlying AlInP layer beneath the oxides remained at 1.45 eV, signifying that the Fermi level was pinned at the same position in both scenarios. The VBO at the oxide/AlInP interface, resulting from the oxidation of the In-rich surface is measured of 1.85 eV after the 20 kL water exposure and increased to 2.35 eV after the extended exposure to O_2. These values are lower than the VBO measured at the interface formed by oxidizing the P-rich AlInP surface. DFT calculations showed that water absorbs more favorably on the In-rich AlInP surface compared to the P-rich surface. The dissociation of water on the In-rich AlInP surface resembles the dissociation process observed in the InP system, leading to OH bonding at In–In bonds and H bonding to the top P dangling bond. Similar energy barriers as the ones present for InP are expected for the AlInP surface that may hinder the reactions. At the same time, the water/surface interface is expected to reduce the energy barriers and further enhance dissociative adsorption.

Overall, the surface chemistry is strongly reconstruction-dependent (subsurface-Al-driven hydroxylation/oxidation on P-rich *versus* In–In-driven reactivity on In-rich), whereas the underlying AlInP band bending converges to a similar pinned state after oxidation. These findings provide a reconstruction-based framework for anticipating early-stage oxidation/hydroxylation and resulting interfacial band offsets in AlInP-based III–V heterostructures under conditions relevant to ALD processing and photoelectrochemical operation. While the band diagrams of oxidized P-rich and In-rich AlInP surfaces are largely similar, the key distinction lies in the nature of the oxide-induced surface states, which may significantly affect charge transport. At the same time, certain oxides such as Al–O–Al could enhance structural stability against corrosion, suggesting that their role should be examined further. Due to the intricate nature of chemical compounds and diversity of reaction sites, such studies are experimentally challenging and difficult to interpret, thus necessitating the integration of calculations with experimental data to enhance understanding.

4 Methodology

4.1 Experimental part

4.1.1 Sample preparation. Following the epilayer preparation reported in ref. 16, a horizontal MOVPE reactor (Aixtron, AIX-200) at a pressure of 100 mbar were employed. H_2 was used as the carrier gas. For substrates, n-GaAs (001) wafers (Si-doped, 2×10^{18} cm^{-3}) with a 0.1° miscut toward the [111] direction are employed. *Tert*-butylarsine (TBAs), trimethylgallium (TMGa), *tert*-butylphosphine (TBP), trimethylindium (TMIn), and trimethylaluminium (TMAl) were used as precursors. Di-*tert*-butylsilane (DTBSi) was utilized as a precursor for Si for n-type doping of samples. The AlInP layer is doped to a relatively high level of 8×10^{18} cm^{-3}, chosen to match the doping levels found in window layer of device structures.[2,14] P- and In-rich AlInP surfaces were prepared as detailed in ref. 16, by post annealing at 310 °C and 440 °C, respectively. RAS (LayTec) as a highly surface-sensitive method[40] were used to *in situ* monitor all MOVPE processes. A mobile UHV shuttle with a base pressure of $<5 \times 10^{-10}$ mbar were utilized for transferring the sample from the MOVPE reactor to UHV-based characterization stations and exposure chamber.[74]

4.1.2 Exposure setup. One of the chambers in the UHV-cluster with a base pressure of 1×10^{-10} mbar is equipped with a leak valve connected to a water reservoir. The absorbent dosage can be accurately regulated by adjusting the chamber pressure by the leak valve. A stress-free window is installed in the chamber, enabling the integration of an RA spectrometer for the *in situ* monitoring of surface modifications. Before and after the exposure experiments, samples were characterized with XPS and UPS, which is located within the same UHV-cluster as the exposure chamber. To prolong O_2 exposure on the In-rich surface, the sample was stored for 2 days in a transfer rod which was equipped with a gate and connection to a pure O_2 cylinder where the pressure of the closed rod could rise to 10^3 mbar.

For water and heat exposure experiments, the ALD chamber is used to introduce water pulses while heating the sample to 200 °C. Before and after 5, 30, and 100 water pulses, XPS, UPS, and tr-2PPE were conducted.

4.1.3 Characterization techniques. Samples were measured by a calibrated XP spectrometer (Specs Focus 500/Phoibos 150/1D-DLD-43-100, monochromatic Al-Kα line). For the UPS measurements, the same spectrometer is used, utilizing He I and He II excitations, which are provided by a Helium gas discharge lamp with energies of 21.22 eV and 40.81 eV, respectively.

In tr-2PPE, electrons originating from occupied electronic states near the surface, typically from the VB or surface states located within the band gap, are photoexcited by means of a pump pulse. As shown in Fig. S16 in the SI, these so-called "hot" electrons subsequently relax towards the CBM, followed by transitions to mid-gap surface states and the VB. *Via* a computer-controlled delay stage, a probe pulse is incident after a time delay Δt. Electrons are photoemitted by this probe pulse, and their measurement is carried out using a time-of-flight (TOF) spectrometer. The time delay Δt is scanned over a range extending to several picoseconds or more, with positive time delays indicating the pump pulse preceding the probe pulse and negative delays denoting the reverse sequence. This excitation and measurement sequence is shown schematically in Fig. S16. In the measurements presented in this study, both the pump and probe are set to 4.49 eV photon energy to allow for photoexcitation across the AlInP band gap and for photoemission of conduction band electrons. The IMFP of photoelectrons in tr-2PPE approximates 2–7 nm,[71,73] enabling observation of emissions from both the surface and near-surface regions, while effectively suppressing bulk signal contributions. This capability allows for the examination of electron dynamics within unoccupied CB or band gap states in the near-surface region; these dynamics remain inaccessible with single-photon spectroscopic methods, such as XPS and UPS.[13,75,76] Comprehensive details on the experimental parameters and an in-depth introduction to tr-2PPE can be found in ref. 71 and the SI.

4.2 Calculations

The total-energy and electronic structure calculations are performed within DFT using the Vienna *Ab initio* Simulation Package (VASP).[77] The projected-augmented-wave (PAW) method[78,79] is used to describe the electron–ion interaction. The wave functions are expanded into plane-waves up to an energy cut-off of 500 eV. The electron exchange correlation energy is calculated within the General Gradient Approximation (GGA) using the PBE functional.[80] The semi-infinite crystal are simulated by a slab consisting of 14 atomic layers and a vacuum layer of ∼15 Å. The bottom of the slab is terminated with partially charged hydrogen atoms ($Z = 1.25$). In order to avoid spurious interaction in the vacuum region a dipole correction normal to the surface is implemented. The Brillouin zone is integrated using a proportional Γ centered k-point mesh of $8 \times 8 \times 1$ per a (1×1) unit cell.

All structures are considered to be structurally relaxed when the forces acting on the atoms are lower than 2 meV Å^{-1}. Potential energy surface calculations were performed to determine the most favorable adsorption sites for low coverages. The potential energy surfaces were sampled at 50 and 64 equidistant mesh points for the (2×4) and (2×2) unit cells, respectively. At each mesh point, three different starting configurations are probed for the water molecule adsorption. Here, the oxygen lateral degrees of freedom parallel to the surface are constrained, while other degrees of freedom are allowed to relax.

The adsorption energy, for each individual site is calculated as

$$E_{\mathrm{ads}} = E_{\mathrm{A+surf}} - E_{\mathrm{surf}} - E_{\mathrm{A}} \quad (2)$$

where $E_{\mathrm{A+surf}}$ is the total energy of the system after adsorption of an adsorbate A on the surface, E_{surf} and E_{A} are the total energies of the clean surface and adsorbate, respectively. The adsorption energy describes the energy difference with respect to a reservoir of water molecules, therefore, E_{A} is referenced to the total energy of a water molecule. For the potential energy surface calculations of a single water molecule the adsorbate energy is simply the total energy of a free water molecule, *i.e.*, $E_{\mathrm{A}} = E_{\mathrm{H_2O}}$.

Detailed descriptions of the AIMD calculations are available in the SI.

Conflicts of interest

The authors declare no conflict of interest.

Data availability

Supporting experimental data and computational results are provided in the supplementary information (SI). The complete raw datasets, including XPS, UPS, RAS, time-resolved 2PPE measurements, as well as DFT and molecular dynamics data, are available in a public repository at https://doi.org/10.5281/zenodo.18367364.

Supplementary information: additional supporting experimental and computational (DFT and AIMD) results, discussion, and schematics of the 2PPE principle. See DOI: https://doi.org/10.1039/d6ta00726k.

Acknowledgements

We gratefully acknowledge the financial support of the German Research Foundation (DFG) through project PAK 981 (project numbers HA3096/14-1, SCHM1361/33, FR 4025/2-1, and KR4816/1-1). Authors are grateful for funding from the Federal Ministry of Research, Technology and Space (BMFTR) through the H2Demo project (project number 03SF0619). M. Z. and A. P. acknowledge funding from the BMFTR through SINATRA: PARASOL project (project number 033RC037). C. D. and T. H. also gratefully acknowledge the financial support of Carl-Zeiss-Stiftung through project "SustEntMat." The authors express their gratitude to Antonio Müller for providing technical assistance throughout the series of experiments and transferring samples between institutes. I. A. R. A. and W. G. S. thank the Paderborn Center for Parallel Computing (PC2) for grants of high-performance computing time.

References

1 J. F. Geisz, R. M. France, K. L. Schulte, M. A. Steiner, A. G. Norman, H. L. Guthrey, M. R. Young, T. Song and T. Moriarty, Six-junction III–V solar cells with 47.1% conversion efficiency under 143 Suns concentration, *Nat. Energy*, 2020, **5**(4), 326–335, DOI: 10.1038/s41560-020-0598-5.

2 H. Helmers, E. Lopez, O. Höhn, D. Lackner, J. Schön, M. Schauerte, M. Schachtner, F. Dimroth and A. W. Bett, 68.9% efficient GaAs-Based photonic power conversion enabled by photon recycling and optical resonance, *Phys. Status Solidi RRL*, 2021, **15**(7), 1–7, DOI: 10.1002/pssr.202100113.

3 P. Schygulla, R. Müller, O. Höhn, M. Schachtner, D. Chojniak, A. Cordaro, S. Tabernig, B. Bläsi, A. Polman, G. Siefer, D. Lackner and F. Dimroth, Wafer-bonded two-terminal III-V//Si triple-junction solar cell with power conversion efficiency of 36.1% at AM1.5g, *Prog. Photovoltaics Res. Appl.*, 2024, 1–9, DOI: 10.1002/pip.3769.

4 National Renewable Energy Laboratory, Best research-cell efficiency chart, https://www.nrel.gov/pv/cell-efficiency.html, accessed: 2024.

5 M. A. Green, E. D. Dunlop, M. Yoshita, N. Kopidakis, K. Bothe, G. Siefer, D. Hinken, M. Rauer, J. Hohl-Ebinger and X. Hao, Solar cell efficiency tables (Version 64), *Prog.*

Photovoltaics Res. Appl., 2024, **32**(7), 425–441, DOI: 10.1002/PIP.3831.

6 M. Klitzke, P. Schygulla, C. Klein, P. Kleinschmidt, T. Hannappel and D. Lackner, Optimization of GaInP Absorber Design for Indoor Photovoltaic Conversion Efficiency above 40%, *Appl. Phys. Lett.*, 2025, **127**(2), 023301, DOI: 10.1063/5.0277001.

7 L. Meier, Ch. Braun, T. Hannappel and W. G. Schmidt, Band Alignment at $Ga_xIn_{1-x}P/Al_yIn_{1-y}P$ Alloy Interfaces from Hybrid Density Functional Theory Calculations, *Phys. Status Solidi B*, 2021, **258**, 2000463, DOI: 10.1002/pssb.202000463.

8 M. M. May, H. J. Lewerenz, D. Lackner, F. Dimroth and T. Hannappel, Efficient direct solar-to-hydrogen conversion by in situ interface transformation of a tandem structure, *Nat. Commun.*, 2015, **6**, 1–7, DOI: 10.1038/ncomms9286.

9 W. H. Cheng, M. H. Richter, M. M. May, J. Ohlmann, D. Lackner, F. Dimroth, T. Hannappel, H. A. Atwater and H. J. Lewerenz, Monolithic photoelectrochemical device for direct water splitting with 19% efficiency, *ACS Energy Lett.*, 2018, **3**(8), 1795–1800, DOI: 10.1021/acsenergylett.8b00920.

10 W. H. Cheng, M. H. Richter, R. Müller, M. Kelzenberg, S. Yalamanchili, P. R. Jahelka, A. N. Perry, P. C. Wu, R. Saive, F. Dimroth, B. S. Brunschwig, T. Hannappel and H. A. Atwater, Integrated Solar-Driven Device with a Front Surface Semitransparent Catalysts for Unassisted CO_2 Reduction, *Adv. Energy Mater.*, 2022, **12**(36), 2201062, DOI: 10.1002/aenm.202201062.

11 U. Würfel, A. Cuevas and P. Würfel, Charge carrier separation in solar cells, *IEEE J. Photovoltaics*, 2014, **5**, 461–469, DOI: 10.1109/JPHOTOV.2014.2363550.

12 M. Schleuning, I. Y. Ahmet, R. van de Krol and M. M. May, The role of selective contacts and built-in field for charge separation and transport in photoelectrochemical devices, *Sustainable Energy Fuels*, 2022, **6**, 3701–3716, DOI: 10.1039/d2se00562j.

13 T. Hannappel, S. Shekarabi, W. Jaegermann, E. Runge, J. P. Hofmann, R. van de Krol, M. M. May, A. Paszuk, F. Hess, A. Bergmann, A. Bund, C. Cierpka, C. Dreßler, F. Dionigi, D. Friedrich, M. Favaro, S. Krischok, M. Kurniawan, K. Lüdge, Y. Lei, B. Roldan Cuenya, P. Schaaf, R. Schmidt-Grund, W. G. Schmidt, P. Strasser, E. Unger, M. F. Vasquez Montoya, D. Wang and H. Zhang, Integration of Multijunction Absorbers and Catalysts for Efficient Solar-Driven Artificial Leaf Structures: A Physical and Materials Science Perspective, *Sol. RRL*, 2024, 1–49, DOI: 10.1002/solr.202301047.

14 D. L. Lepkowski, T. Kasher, J. T. Boyer, D. J. Chmielewski, T. J. Grassman and S. A. Ringel, The critical role of AlInP window design in III-V rear-emitter solar cells, *IEEE J. Photovoltaics*, 2020, **10**(3), 758–764, DOI: 10.1109/JPHOTOV.2020.2978863.

15 L. J. Glahn, I. A. Ruiz Alvarado, S. Neufeld, M. A. Zare Pour, A. Paszuk, D. Ostheimer, S. Shekarabi, O. Romanyuk, D. C. Moritz, J. P. Hofmann, W. Jaegermann, T. Hannappel and W. G. Schmidt, Clean and hydrogen-adsorbed AlInP(001) surfaces: structures and electronic properties, *Phys. Status Solidi B*, 2022, **259**(11), 2200308, DOI: 10.1002/pssb.202200308.

16 M. A. Zare Pour, S. Shekarabi, I. A. Ruiz Alvarado, J. Diederich, Y. Gao, A. Paszuk, D. C. Moritz, W. Jägermann, D. Friedrich, R. van de Krol, W. G. Schmidt and T. Hannappel, Exploring Electronic States and Ultrafast Electron Dynamics in AlInP Window Layers: The Role of Surface Reconstruction, *Adv. Funct. Mater.*, 2025, 2423702, DOI: 10.1002/adfm.202423702.

17 J. L. A. Alves, J. Hebenstreit and M. Scheffler, Calculated atomic structures and electronic properties of GaP, InP, GaAs, and InAs (110) surfaces, *Phys. Rev. B:Condens. Matter Mater. Phys.*, 1991, **44**(12), 6188–6198, DOI: 10.1103/PhysRevB.44.6188.

18 P. H. Hahn and W. G. Schmidt, Surface ordering of P-rich InP(001): Hydrogen stabilization vs electron correlation, *Surf. Rev. Lett.*, 2003, **10**, 163–167, DOI: 10.1142/s0218625x03004913.

19 H. Katayama-Yoshida and K. Sato, Materials design for semiconductor spintronics by ab initio electronic-structure calculation, *Phys. Rev. B:Condens. Matter Mater. Phys.*, 2003, **327**(2–4), 337–343, DOI: 10.1016/S0921-4526(02)01782-9.

20 L. H. Yu, K. L. Yao and Z. L. Liu, Electronic band structures of filled tetrahedral semiconductor LiMgP and zinc-blende AlP, *Solid State Commun.*, 2005, **135**(1–2), 124–128, DOI: 10.1016/J.SSC.2005.03.041.

21 N. G. C. Astrath, F. Sato, F. Pedrochi, A. N. Medina, A. C. Bento, M. L. Baesso, C. Persson and A. F. Da Silva, Band gap energy determination by photoacoustic spectroscopy under continuous light excitation, *Appl. Phys. Lett.*, 2006, **89**(23), 231926, DOI: 10.1063/1.2402239.

22 T. M. Christian, D. A. Beaton, K. Mukherjee, K. Alberi, E. A. Fitzgerald and A. Mascarenhas, Amber-Green Light-Emitting Diodes Using Order–Disorder Al\(x\)In\(1−x\)P Heterostructures, *J. Appl. Phys.*, 2013, **114**(7), 074505, DOI: 10.1063/1.4818477.

23 K. Mukherjee, D. A. Beaton, T. Christian, E. J. Jones, K. Alberi, A. Mascarenhas, M. T. Bulsara and E. A. Fitzgerald, Growth, microstructure, and luminescent properties of direct-bandgap InAlP on relaxed InGaAs on GaAs substrates, *J. Appl. Phys.*, 2013, **113**, 183518, DOI: 10.1063/1.4804264.

24 M. Vaisman, K. Mukherjee, T. Masuda, K. N. Yaung, E. A. Fitzgerald, and M. L. Lee, Direct-gap 2.1–2.2 eV AlInP solar cells on GaInAs/GaAs metamorphic buffers, in *2015 IEEE 42nd PVSC*, Portland, OR, USA, 2015, DOI: 10.1109/PVSC.2015.7356435.

25 S. Hu, C. Xiang, S. Haussener, A. D. Berger and N. S. Lewis, An analysis of the optimal band gaps of light absorbers in integrated tandem photoelectrochemical water-splitting systems, *Energy Environ. Sci.*, 2013, **6**(10), 2984–2993, DOI: 10.1039/C3EE40453F.

26 T. F. Rieth, V. Streibel, O. Bienek, S. Levashov, J. Dittloff, K. Möller, J. Eichhorn, M. M. May and I. D. Sharp, Enhancing Direct Solar Water Splitting via ALD of Multifunctional TiO_2/Pt Nanoparticle Coatings With

Engineered Interfaces to GaAs/GaInP Tandem Cells, *Adv. Funct. Mater.*, 2025, e05106, DOI: 10.1002/adfm.202505106.

27 B. C. Wood, T. Ogitsu and E. Schwegler, Local structural models of complex oxygen- and hydroxyl-rich GaP/InP(001) surfaces, *J. Chem. Phys.*, 2012, **136**(6), 064705, DOI: 10.1063/1.3682768.

28 B. C. Wood, E. Schwegler, W. I. Choi and T. Ogitsu, Hydrogen-bond dynamics of water at the interface with InP/GaP(001) and the implications for photoelectrochemistry, *J. Am. Chem. Soc.*, 2013, **135**(42), 15774–15783, DOI: 10.1021/ja403850s.

29 B. C. Wood, E. Schwegler, W. I. Choi and T. Ogitsu, Surface chemistry of GaP(001) and InP(001) in contact with water, *J. Phys. Chem. C*, 2014, **118**(2), 1062–1070, DOI: 10.1021/jp4098843.

30 S. Jeon, H. Kim, W. A. Goddard and H. A. Atwater, DFT study of water adsorption and decomposition on a Ga-rich GaP(001)(2×4) surface, *J. Phys. Chem. C*, 2012, **116**(33), 17604–17612, DOI: 10.1021/jp3041555.

31 I. A. Ruiz Alvarado and W. G. Schmidt, Water/InP(001) from Density Functional Theory, *ACS Omega*, 2022, **7**(23), 19355–19364, DOI: 10.1021/acsomega.2c00948.

32 I. A. Ruiz Alvarado, M. Karmo, E. Runge and W. G. Schmidt, InP and AlInP(001)(2×4) surface oxidation from density functional theory, *ACS Omega*, 2021, **6**(9), 6297–6304, DOI: 10.1021/acsomega.0c06019.

33 D. C. Moritz, I. A. Ruiz Alvarado, M. A. Zare Pour, A. Paszuk, T. Frieß, E. Runge, J. P. Hofmann, T. Hannappel, W. G. Schmidt and W. Jaegermann, P-terminated InP (001) surfaces: surface band bending and reactivity to water, *ACS Appl. Mater. Interfaces*, 2022, **14**(41), 47255–47261, DOI: 10.1021/acsami.2c13352.

34 O. Henrion, A. Klein and W. Jaegermann, Water adsorption on UHV cleaved InP(110) surfaces, *Surf. Sci.*, 2000, **457**(1), 337–341, DOI: 10.1016/S0039-6028(00)00417-9.

35 M. May, H. J. Lewerenz and T. Hannappel, Optical in situ study of InP(100) surface chemistry: Dissociative adsorption of water and oxygen, *J. Phys. Chem. C*, 2014, **118**(33), 19032–19041, DOI: 10.1021/jp502955m.

36 D. Ostheimer, C. Dreßler, M. Grossmann, M. A. Zare Pour, S. Shekarabi, K. D. Hanke, J. Koch, A. Paszuk, E. Runge and T. Hannappel, Water Vapor Interaction with Well-Ordered GaInP(100) Surfaces, *J. Phys. Chem. C*, 2024, **128**, 19559–19569, DOI: 10.1021/acs.jpcc.4c04597.

37 A. Hajduk, M. V. Lebedev, B. Kaiser and W. Jaegermann, Interaction of liquid water with the p-GaInP$_2$(100) surface covered with submonolayer oxide, *Phys. Chem. Chem. Phys.*, 2018, **20**(32), 21144–21150, DOI: 10.1039/c8cp03337d.

38 M. A. Zare Pour, O. Romanyuk, D. C. Moritz, A. Paszuk, C. Maheu, S. Shekarabi, K. D. Hanke, D. Ostheimer, T. Mayer, J. P. Hofmann, W. Jaegermann and T. Hannappel, Band energy diagrams of n-GaInP/n-AlInP(100) surfaces and heterointerfaces studied by X-ray photoelectron spectroscopy, *Surf. Interfaces*, 2022, **34**, 102384, DOI: 10.1016/J.SURFIN.2022.102384.

39 I. A. Ruiz Alvarado, M. A. Zare Pour, T. Hannappel and W. G. Schmidt, Structural fingerprints in the reflectance anisotropy of AlInP(001), *Phys. Rev. B*, 2023, **108**(4), 045410, DOI: 10.1103/PhysRevB.108.045410.

40 M. M. May, O. Supplie, C. Höhn, R. Van De Krol, H. J. Lewerenz and T. Hannappel, The interface of GaP(100) and H_2O studied by photoemission and reflection anisotropy spectroscopy, *New J. Phys.*, 2013, **15**, 1–17, DOI: 10.1088/1367-2630/15/10/103003.

41 S. E. Acosta-Ortiz and A. Lastras-Martínez, Electro-optic effects in the optical anisotropies of (001) GaAs, *Phys. Rev. B:Condens. Matter Mater. Phys.*, 1989, **40**(2), 1426–1429, DOI: 10.1103/PhysRevB.40.1426.

42 D. T. Clark, T. Fok, G. G. Roberts and R. W. Sykes, An investigation by electron spectroscopy for chemical analysis of chemical treatments of the (100) surface of n-type InP epitaxial layers for Langmuir film deposition, *Thin Solid Films*, 1980, **70**(2), 261–283, DOI: 10.1016/0040-6090(80)90367-3.

43 J. A. Taylor, An XPS study of the oxidation of AlAs thin films grown by MBE, *J. Vac. Sci. Technol.*, 1982, **20**(3), 751–755, DOI: 10.1116/1.571450.

44 H. J. Levinson, F. Greuter and E. W. Plummer, Experimental Band Structure of Aluminum, *Phys. Rev. B:Condens. Matter Mater. Phys.*, 1983, **27**, 727–738, DOI: 10.1103/PhysRevB.27.727.

45 M. Faur, D. T. Jayne, M. Goradia and C. Goradia, XPS investigation of anodic oxides grown on p-type InP, *Surf. Interface Anal.*, 1990, **15**(11), 641–650.

46 H. He, K. Alberti, T. L. Barr and J. Klinowski, ESCA Studies of Aluminophosphate Molecular Sieves, *J. Phys. Chem.*, 1993, **97**(51), 13703–13707, DOI: 10.1021/j100153a045.

47 T. Lindblad, B. Rebenstorf, Z.-G. Yan and S. L. T. Andersson, Characterization of vanadia supported on amorphous $AlPO_4$ and its properties for oxidative dehydrogenation of propane, *Appl. Catal., A*, 1994, **112**(2), 187–208, DOI: 10.1016/0926-860X(94)80219-X.

48 F. Rueda, J. Mendialdua, A. Rodriguez, R. Casanova, Y. Barbaux, L. Gengembre and L. Jalowiecki, Characterization of Venezuelan laterites by X-ray photoelectron spectroscopy, *J. Electron Spectrosc. Relat. Phenom.*, 1996, **82**(3), 135–143, DOI: 10.1016/S0368-2048(96)03035-6.

49 S.-L. Chang, J. W. Anderegg and P. A. Thiel, Surface oxidation of an Al–Pd–Mn quasicrystal, characterized by X-ray photoelectron spectroscopy, *J. Non-Cryst. Solids*, 1996, **195**(1–2), 95–101, DOI: 10.1016/0022-3093(95)00537-4.

50 Y. Muraoka and K. Kihara, The temperature dependence of the crystal structure of berlinite, a quartz-type form of AlPO\(4\), *Phys. Chem. Miner.*, 1997, **24**, 243–253, DOI: 10.1007/s002690050036.

51 I. Costina and R. Franchy, Band gap of amorphous and well-ordered Al\(2\)O\(3\) on Ni\(3\)Al(100), *Appl. Phys. Lett.*, 2001, **78**(26), 4139–4141, DOI: 10.1063/1.1380403.

52 Z. Li, Z. Xie, Y. Zhang, L. Wu, X. Wang and X. Fu, Wide Band Gap p-Block Metal Oxyhydroxide InOOH: A New Durable Photocatalyst for Benzene Degradation, *J. Phys. Chem. C*, 2007, **111**(49), 18348–18352, DOI: 10.1021/jp076107r.

53 A. Alemi, Z. Hosseinpour, M. Dolatyari and A. Bakhtiari, Boehmite (γ-AlOOH) Nanoparticles: Hydrothermal Synthesis, Characterization, pH-Controlled Morphologies, Optical Properties, and DFT Calculations, *Phys. Status Solidi B*, 2012, **249**(6), 1264–1270, DOI: 10.1002/pssb.201147484.

54 S. Ge, B. Wang, J. Lin and L. Zhang, C,N-Codoped InOOH Microspheres: One-Pot Synthesis, Growth Mechanism and Visible Light Photocatalysis, *CrystEngComm*, 2013, **15**(4), 721–728, DOI: 10.1039/C2CE26373D.

55 E. O. Filatova and A. S. Konashuk, Interpretation of the Changing the Band Gap of Al\(2\)O\(3\) Depending on Its Crystalline Form: Connection with Different Local Symmetries, *J. Phys. Chem. C*, 2015, **119**(35), 20755–20761, DOI: 10.1021/acs.jpcc.5b06843.

56 X. Zhou, J. Zhang, Y. Ma, H. Tian, Y. Wang, Y. Li, L. Jiang and Q. Cui, The Solvothermal Synthesis of γ-AlOOH Nanoflakes and Their Compression Behaviors Under High Pressures, *RSC Adv.*, 2017, **7**(9), 4904–4911, DOI: 10.1039/C6RA27571K.

57 D. Kim, J. H. Jung and J. Ihm, Theoretical Study of Aluminum Hydroxide as a Hydrogen-Bonded Layered Material, *Nanomaterials*, 2018, **8**(6), 375, DOI: 10.3390/nano8060375.

58 A. Hajduk, M. A. Zare Pour, A. Paszuk, M. Guidat, M. Löw, F. Ullmann, D. C. Moritz, J. P. Hofmann, S. Krischok, E. Runge, W. G. Schmidt, W. Jaegermann, M. M. May and T. Hannappel, (Photo-)electrochemical reactions on semiconductor surfaces, part B: III-V surfaces–atomic and electronic structure, *Encyclopedia of Solid-Liquid Interfaces*, ed. K. Wandelt and G. Bussetti, Elsevier, Oxford, UK, 2024, pp. 120–156, DOI: 10.1016/B978-0-323-85669-0.00113-6.

59 X. Zhang and S. Ptasinska, Dissociative adsorption of water on an H\(2\)O/GaAs(100) interface: In situ near-ambient pressure XPS studies, *J. Phys. Chem. C*, 2014, **118**(8), 4259–4266, DOI: 10.1021/jp411977p.

60 C. D. Wagner, A. V. Naumkin, A. Kraut-Vass, J. W. Allison, C. J. Powell, and J. R. Rumble, *NIST Standard Reference Database 20, Version 3.4 (Web Version)*, National Institute of Standards and Technology, 2003.

61 J. F. Moulder, W. F. Stickle, P. E. Sobol, and K. D. Bomben, *Handbook of X-Ray Photoelectron Spectroscopy*, Perkin-Elmer Corp., Eden Prairie, MN, 1992.

62 S. J. Hoekje and G. B. Hoflund, Surface characterization study of InP(100) substrates using ion-scattering spectroscopy, Auger electron spectroscopy and electron spectroscopy for chemical analysis I: Comparison of substrate-cleaning techniques, *Thin Solid Films*, 1991, **197**(1–2), 367–380, DOI: 10.1016/0040-6090(91)90247-U.

63 J. T. Wolan and G. B. Hoflund, Chemical alteration of the native oxide layer on InP(111) by exposure to hyperthermal atomic hydrogen, *J. Vac. Sci. Technol., A*, 1998, **16**(4), 2546–2552, DOI: 10.1116/1.581379.

64 G. Chen, S. B. Visbeck, D. C. Law and R. F. Hicks, Structure-sensitive oxidation of the indium phosphide (001) surface, *J. Appl. Phys.*, 2002, **91**(11), 9362–9367, DOI: 10.1063/1.1471577.

65 T. Barr, J. Klinowski, H. He and K. Alberti, Evidence for strong acidity of the molecular sieve cloverite, *Nature*, 1993, **365**, 429–431, DOI: 10.1038/365429a0.

66 M. A. Zare Pour, M. N. Qaisrani, C. Höhn, J. L. Wolf, N. Mogharehabed, J. Velazquez Rojas, W. Jaegermann, E. Runge, R. van de Krol, T. Hannappel, C. Dreßler and A. Paszuk, Composition and Resulting Band Alignment at the TiO_2/InP Heterointerface: A Fundamental Study Combining Photoemission Spectroscopy and Theory, *Adv. Funct. Mater.*, 2025, 2506105, DOI: 10.1002/adfm.202506105.

67 W. Jaegermann and T. Mayer. 3.8.2 H\(2\)O and OH on Semiconductors - Text and Tables. in *Landolt-Börnstein - Group III Condensed Matter, Vol. 42A4, Adsorbed Layers on Surfaces*, ed. H. P. Bonzel, Springer-Verlag, Berlin Heidelberg, 2005, DOI: 10.1007/10932216_6.

68 C. U. S. Larsson and A. S. Flodström, Dissociative H\(2\)O adsorption on the Si(100) 2× 1 and Ge(100) 2× 1 surfaces, *Vacuum*, 1991, **42**(4), 297–300, DOI: 10.1016/0042-207X(91)90041-G.

69 X. Zhang, T. Ogitsu, B. C. Wood, T. A. Pham and S. Ptasinska, Oxidation-Induced Polymerization of InP Surface and Implications for Optoelectronic Applications, *J. Phys. Chem. C*, 2019, **123**(51), 30893–30902, DOI: 10.1021/acs.jpcc.9b07260.

70 S. Trasatti, The absolute electrode potential: an explanatory note, *Pure Appl. Chem.*, 1986, **58**(7), 955–966, DOI: 10.1351/pac198658070955.

71 J. Diederich, J. V. Rojas, M. A. Zare Pour, I. A. Ruiz Alvarado, A. Paszuk, R. Sciotto, C. Höhn, K. Schwarzburg, D. Ostheimer, R. Eichberger, W. G. Schmidt, T. Hannappel, R. van de Krol and D. Friedrich, Unraveling electron dynamics in p-type indium phosphide (100): A time-resolved two-photon photoemission study, *J. Am. Chem. Soc.*, 2024, **146**(13), 8949–8960, DOI: 10.1021/jacs.3c12487.

72 J. Diederich, A. Paszuk, I. A. Ruiz Alvarado, M. Krenz, M. A. Zare Pour, D. S. Babu, J. Velazquez Rojas, C. Höhn, Y. Gao, K. Schwarzburg, D. Ostheimer, R. Eichberger, W. G. Schmidt, T. Hannappel, R. van de Krol and D. Friedrich, Ultrafast Electron Dynamics at the Water-Modified InP(100) Surface, *Adv. Mater. Interfaces*, 2025, e00463, DOI: 10.1002/admi.202500463.

73 M. P. Seah and W. A. Dench, Quantitative electron spectroscopy of surfaces: A standard data base for electron inelastic mean free paths in solids, *Surf. Interface Anal.*, 1979, **1**(1), 2–11, DOI: 10.1002/SIA.740010103.

74 T. Hannappel, S. Visbeck, L. Töben and F. Willig, Apparatus for investigating metalorganic chemical vapor deposition-grown semiconductors with ultrahigh-vacuum based techniques, *Rev. Sci. Instrum.*, 2004, **75**(5), 1297–1304, DOI: 10.1063/1.1711148.

75 H. Ueba and B. Gumhalter, Theory of two-photon photoemission spectroscopy of surfaces, *Prog. Surf. Sci.*, 2007, **82**(4–6), 193–223, DOI: 10.1016/J.PROGSURF.2007.03.002.

76 M. Borgwardt, S. T. Omelchenko, M. Favaro, P. Plate, C. Höhn, D. Abou-Ras, K. Schwarzburg, R. van de Krol,

H. A. Atwater, N. S. Lewis, R. Eichberger and D. Friedrich, Femtosecond time-resolved two-photon photoemission studies of ultrafast carrier relaxation in Cu_2O photoelectrodes, *Nat. Commun.*, 2019, **10**(1), 1–7, DOI: 10.1038/s41467-019-10143-x.

77 G. Kresse and J. Furthmüller, Efficiency of ab-initio total energy calculations for metals and semiconductors using a plane-wave basis set, *Comput. Mater. Sci.*, 1996, **6**(1), 15–50, DOI: 10.1016/0927-0256(96)00008-0.

78 P. E. Blöchl, Projector augmented-wave method, *Phys. Rev. B:Condens. Matter Mater. Phys.*, 1994, **50**(24), 17953–17979, DOI: 10.1103/PhysRevB.50.17953.

79 G. Kresse and D. Joubert, From ultrasoft pseudopotentials to the projector augmented-wave method, *Phys. Rev. B:Condens. Matter Mater. Phys.*, 1999, **59**(3), 1758–1775, DOI: 10.1103/PhysRevB.59.1758.

80 J. P. Perdew, K. Burke and M. Ernzerhof, Generalized gradient approximation made simple, *Phys. Rev. Lett.*, 1996, **77**(18), 3865–3868, DOI: 10.1103/PhysRevLett.77.3865.